

# Photospheric Electric Fields and Energy Fluxes in the Eruptive Active Region NOAA 11158

Maria D. Kazachenko<sup>1</sup>, George H. Fisher<sup>1</sup>, Brian T. Welsch<sup>1</sup>, Xudong Sun<sup>2</sup>, Yang Liu<sup>2</sup>

kazachenko@ssl.berkeley.edu

Received \_\_\_\_\_; accepted \_\_\_\_\_

---

<sup>1</sup>Space Sciences Laboratory, UC Berkeley

<sup>1</sup>Stanford University

## ABSTRACT

How much electromagnetic energy crosses the photosphere in evolving solar active regions? With the advent of high-cadence vector magnetic field observations, addressing this fundamental question has become tractable. In this paper, we apply the “PTD-Doppler-FLCT-Ideal” (PDFI) electric field inversion technique of Kazachenko et al. (2014) to a 6-day HMI/SDO vector magnetogram and Doppler velocity sequence, to find the electric field and Poynting flux evolution in NOAA active region 11158, which produced an X2.2 flare early on 2011 February 15. We find photospheric electric fields ranging up to 1.5 V/cm. The Poynting fluxes range up to  $2 \times 10^{10}$  ergs·cm<sup>-2</sup>s<sup>-1</sup> with mean values around  $10^8$ – $10^9$  ergs·cm<sup>-2</sup>s<sup>-1</sup>. Integrating the instantaneous energy flux over space and time, we find that the total magnetic energy accumulated above the photosphere from emergence to the moment before the X2.2 flare to be  $E = 10.6 \times 10^{32}$  ergs, which is partitioned as 2.0 and  $8.6 \times 10^{32}$  ergs, respectively, between free and potential energies. Those estimates are consistent with estimates from pre-flare non-linear force-free field (NLFFF) extrapolations and the Minimum Current Corona estimates (MCC), in spite of our very different approach. This study of photospheric electric fields demonstrates the potential of the PDFI approach for estimating Poynting fluxes and opens the door to more quantitative studies of the solar photosphere and more realistic data-driven simulations of coronal magnetic field evolution.

*Subject headings:* Sun: magnetic field, Sun: flares, Sun: sunspots

## Contents

<b>1</b>	<b>INTRODUCTION</b>	<b>1</b>
<b>2</b>	<b>METHODOLOGY: PDFI TECHNIQUE, POYNTING &amp; HELICITY FLUXES</b>	<b>4</b>
<b>3</b>	<b>DATA REDUCTION: AR 11158</b>	<b>8</b>
3.1	Deriving Magnetic Vector Fields: $\mathbf{B}$ . . . . .	8
3.2	Deriving Velocity Vector Fields: $\mathbf{V}$ . . . . .	11
3.3	How do Errors in Magnetic Field Measurements Affect our Electric Fields? .	12
<b>4</b>	<b>RESULTS</b>	<b>15</b>
4.1	Properties Of the Active Region AR 11158 Before and After the X2.2 Flare .	15
4.1.1	Magnetic Field: $\mathbf{B}_{\text{pre}}$ and $\mathbf{B}_{\text{post}}$ . . . . .	15
4.1.2	Velocity Field: $\mathbf{V}_{\text{pre}}$ and $\mathbf{V}_{\text{post}}$ . . . . .	16
4.1.3	Electric Field: $\mathbf{E}_{\text{pre}}$ and $\mathbf{E}_{\text{post}}$ . . . . .	17
4.1.4	Poynting Flux Vector: $\mathbf{S}_{\text{pre}}$ and $\mathbf{S}_{\text{post}}$ . . . . .	19
4.2	Six-Day Evolution of Vertical Energy and Helicity Fluxes . . . . .	21
4.2.1	Evolution of Free, Potential, and Total Poynting Fluxes . . . . .	21
4.2.2	Helicity Flux Evolution . . . . .	23
<b>5</b>	<b>DISCUSSION</b>	<b>28</b>

<b>6</b>	<b>CONCLUSION</b>	<b>33</b>
<b>A</b>	<b>SCALING B AND E TO CARTESIAN MERCATOR MESH</b>	<b>38</b>

## 1. INTRODUCTION

The advent of high-cadence, large-scale vector magnetic field and Doppler velocity measurements from instruments such as the Helioseismic and Magnetic Imager (HMI, Schou et al. (2012)) on NASA’s Solar Dynamics Observatory (SDO) satellite (Pesnell et al. 2012), the Spectropolarimeter instrument (SP; Lites et al. 2013) on Solar Optical Telescope (Tsuneta et al. 2008) aboard the *Hinode* satellite (Kosugi et al. 2007), and improved capabilities of ground-based instruments, such as SOLIS (e.g., Keller et al. 2003), make the estimation of electric fields in the solar photosphere possible. The calculation of the electric field from magnetic and Doppler data is critically important for various quantitative studies of the solar atmosphere. First, if we know both electric and magnetic field vectors in the photosphere, we can estimate both the Poynting flux of magnetic energy and the flux of relative magnetic helicity entering the corona. Second, as demonstrated in a magneto-frictional model by Cheung and DeRosa (2012), the ability to compute the electric field enables the driving of time-dependent simulations of the coronal magnetic field from photospheric magnetogram sequences. Combining electric field estimation with a magneto-frictional model of the evolving solar corona is the goal of the Coronal Global Evolutionary Model (CGEM) project.<sup>1</sup>

Kazachenko et al. (2014) modified and extended the electric field inversion methods presented by Fisher et al. (2010, 2012), to create a comprehensive technique for calculating photospheric electric fields from vector magnetogram sequences. The new method, which we dubbed the PDFI (an abbreviation for **P**oloidal-Toroidal Decomposition [PTD]-**D**oppler-**F**ourier Local Correlation Tracking [FLCT]-**I**deal) technique, incorporates Doppler velocities from non-normal viewing angles (which are relevant to most solar observations) and a faster and a more robust Poisson equation solver, for obtaining the PTD solutions. After

---

<sup>1</sup><http://cgem.stanford.edu>

systematic, quantitative tests of the accuracy and robustness of the PDFI technique, using synthetic data from anelastic MHD (ANMHD) simulations (Abbett et al. 2004), we found that the PDFI method has less than 1% error in the total Poynting flux and a 10% error in the helicity flux rate if we reconstruct it at the normal viewing angle ( $\theta = 0$ ) and less than 25% and 10% errors respectively at large viewing angles ( $\theta = 60^\circ$ ) (Kazachenko et al. 2014).

In this paper, we take the next step forward, and apply the PDFI technique to observations. The flare-productive NOAA active region (AR) 11158 was observed by HMI nearly continuously for a six-day period over 10-16 February 2011, starting from its emergence near 14:00 UT on 10 February. We use the sequence of magnetic and Doppler field measurements of AR 11158 to derive the temporal evolution of electric field, Poynting, and helicity fluxes during these six days. The evolution of this AR included two large bipoles emerging in close proximity, with strong shearing motion between the central sunspots (Schrijver et al. 2011; Sun et al. 2012). Over a five-day period, the AR hosted an X2.2 flare (with the GOES soft X-ray flux peaking at 01:56 UT on February 15) leading to a pronounced halo CME, three M-class flares, and over twenty C-class flares. Since this active region was the first one for which the HMI vector magnetic field data were widely distributed to the scientific community, its magnetic field has been thoroughly studied: the fast sunspot rotation from 20 hours before to 1 hour after the X2.2 flare (Jiang et al. 2012; Vemareddy et al. 2012a), the flare related enhancement in the horizontal magnetic field along the magnetic polarity inversion line (PIL; Gosain (2012); Wang et al. (2012); Liu et al. (2012a)), abrupt changes in the vertical Lorentz force vectors (Petrie 2012; Alvarado-Gómez et al. 2012) and horizontal Lorentz forces (Petrie 2013; Wang et al. 2014), the evolution of relative and current magnetic helicities (Jing et al. 2012), the injection of oppositely signed helicity through the photosphere (Dalmasse et al. 2013), the subsurface three-dimensional magnetic structure (Chintzoglou and Zhang 2013), the magnetic and velocity field transients driven by the flare (Maurya et al. 2012), etc. Numerous approaches were used to calculate

the energy associated with X2.2 flare and the AR as a whole: the DAVE4VM method (Liu and Schuck 2012; Tziotziou et al. 2013), non-linear force free extrapolation (Sun et al. 2012; Tziotziou et al. 2013), the Minimum Current Corona Model (Tarr et al. 2013), and the coronal forward-fitting method (Aschwanden et al. 2014; Malanushenko et al. 2014). In this paper, we apply the PDFI technique (Kazachenko et al. 2014) to derive electric fields at the photosphere, and use those to estimate the photospheric energy and helicities fluxes’ evolution in AR 11158.

The paper is structured as follows. In Section 2 we briefly review the PDFI method itself and its recent improvements. In Section 3 we describe the observations of the emerging, flaring AR 11158, and quantify how the uncertainties in the HMI observations propagate into derived electric field and Poynting fluxes. In Section 4, we describe derived electric fields, Poynting, and helicity fluxes in AR 11158, and in Section 5 we discuss results and draw conclusions. In addition, in Appendix A we show how our Mercator-reprojected magnetic fields in Cartesian coordinates can be scaled to apply to relatively small regions on the surface of the Sun to derive the electric fields in a local cartesian coordinate system.

## 2. METHODOLOGY: PDFI TECHNIQUE, POYNTING & HELICITY FLUXES

The PDFI technique uses evolution of the vector magnetic field  $\mathbf{B}$  and horizontal and Doppler velocities  $\mathbf{V}$  to estimate electric fields in the solar photosphere. It is described in detail in §2 of Kazachenko et al. (2014). The PDFI method combines the *inductive* contribution to the electric field  $\mathbf{E}$  from solution to Faraday’s law using the Poloidal-Toroidal-Decomposition (PTD) technique (Fisher et al. 2010, 2012), with *non-inductive* contributions from  $(-\mathbf{V} \times \mathbf{B})$ . To find the velocity  $\mathbf{V}$ , we use Doppler measurements and the Fourier Local Correlation Tracking (FLCT) technique. The PDFI technique is tested and its accuracy is characterized in detail in §4 of Kazachenko et al. (2014). In this section we briefly describe the basics of the PDFI technique.

The fundamental idea of the PTD part of the PDFI method is that the magnetic field,  $\mathbf{B}$ , defined on the photospheric surface, has a solenoidal nature and thus can be specified by two scalar functions  $\mathcal{B}$  and  $\mathcal{J}$ :

$$\mathbf{B} = \nabla \times \nabla \times \mathcal{B} \hat{\mathbf{z}} + \nabla \times \mathcal{J} \hat{\mathbf{z}}, \quad (1)$$

where  $\hat{\mathbf{z}}$  points upward from the photosphere. Taking a partial time derivative of Equation (1), and demanding that  $\mathbf{B}$  obeys Faraday’s law,

$$\frac{\partial \mathbf{B}}{\partial t} = -(\nabla \times c\mathbf{E}), \quad (2)$$

we find a solution for the inductive part of the electric field  $\mathbf{E}^{\mathbf{P}}$  (where “P” stands for PTD), in terms of the partial time derivatives of the poloidal and toroidal potentials,  $\dot{\mathcal{B}}$  and  $\dot{\mathcal{J}}$  respectively, by “uncurling” Equation (2):

$$c\mathbf{E}^{\mathbf{P}} = -\nabla \times \dot{\mathcal{B}} \hat{\mathbf{z}} - \dot{\mathcal{J}} \hat{\mathbf{z}}. \quad (3)$$

Solving two-dimensional Poisson equations in the domain, where we observe the vector magnetic fields, we determine  $\dot{\mathcal{B}}$ ,  $\dot{\mathcal{J}}$  and  $\frac{\partial \dot{\mathcal{B}}}{\partial z}$ . Note that the vector magnetic field data



completely specify the source terms of these Poisson equations, as described in §2.1 of Kazachenko et al. (2014).

The total electric field  $\mathbf{E}$  is a combination of the inductive and non-inductive parts,

$$c\mathbf{E} = -\nabla \times \dot{\mathcal{B}}\hat{\mathbf{z}} - \dot{\mathcal{J}}\hat{\mathbf{z}} - \nabla\psi \equiv \underbrace{c\mathbf{E}^{\mathbf{P}}}_{\text{inductive}} - \underbrace{\nabla\psi}_{\text{non-inductive}}. \quad (4)$$

The non-inductive components to the scalar-potential part of the solution include three separate contributions: (1)  $-\mathbf{V} \times \mathbf{B}$  from Doppler measurements (the “D” in PDFI), (2)  $-\mathbf{V} \times \mathbf{B}$  from Fourier Local Correlation Tracking results (the “F” in PDFI), and (3) a scalar potential contribution added to impose the constraint  $\mathbf{E} \cdot \mathbf{B} = 0$ , consistent with the ideal MHD Ohm’s law (the “I” in PDFI). When adding the  $-\mathbf{V} \times \mathbf{B}$  contributions above, any inductive contributions from these terms are removed, since all inductive contributions are already included in the  $\mathbf{E}^{\mathbf{P}}$  solution. Our approach for handling these non-inductive contributions is described in detail in Kazachenko et al. (2014).

To calculate the flux of electromagnetic energy at the photosphere, given by the Poynting flux vector

$$\mathbf{S} = \frac{c}{4\pi}(\mathbf{E} \times \mathbf{B}), \quad (5)$$

we use the observed magnetic field vector and the electric field vector derived using the PDFI method. Since we are interested in the amount of energy flowing into and out of the corona, we focus most of our attention on the vertical component of Poynting flux,

$$S_z = \frac{c}{4\pi} (E_x B_y - E_y B_x) . \quad (6)$$

This depends upon the horizontal components of both the electric field and the magnetic field. We further decompose  $S_z$  into two contributions, the flux of potential-field energy, and the flux of free magnetic energy. The basic idea is that the horizontal magnetic field  $\mathbf{B}_h$  can be divided into a potential-field contribution  $\mathbf{B}_h^P$ , and a contribution,  $\mathbf{B}_h^f$ ,

due to currents that flow into the atmosphere from the photosphere (Welsch 2006):

$S_z = \frac{c}{4\pi} \mathbf{E}_h \times (\mathbf{B}_h^P + \mathbf{B}_h^f)$ . In this paper we use the Green’s function to find the potential field contribution, and subtract this contribution from the measured horizontal fields to find  $\mathbf{B}_h^f$ . More discussion of the potential and free energy decomposition can be found in §3.1 of Kazachenko et al. (2014).

To calculate helicity flux rates, we use Equation (62) from Berger and Field (1984):

$$\left( \frac{dH_R}{dt} \right) = -2 \int (\mathbf{A}^P \times \mathbf{E}) \cdot \hat{\mathbf{z}} da = -2 \underbrace{\int (A_x^P E_y - A_y^P E_x) da}_{\text{PDFI}}, \quad (7)$$

where  $\mathbf{A}^P = \left( \frac{\partial \mathcal{B}^P}{\partial y}, -\frac{\partial \mathcal{B}^P}{\partial x}, 0 \right) = \nabla \times B^P \hat{\mathbf{z}}$  is the vector potential that generates the potential field  $\mathbf{B}^P$  in volume  $V$ , which matches the photospheric normal field  $B_z$  at  $z = 0$ . (Note that a similar expression for helicity, Equation (41) in Kazachenko et al. (2014), contains a typographical error  $-E_z$  should be replaced by  $E_x$ .) Here  $B^P$  can be found by solving the Poisson equation A5 in Fisher et al. (2010). Adopting the naming convention from §2.3.4 in Kazachenko et al. (2014), the total helicity flux rate derived from the PDFI electric field  $\mathbf{E}$  will be referred to as the PDFI helicity flux rate or  $\left( \frac{dH_R}{dt} \right)_{\text{PDFI}}$ .

If we have an ideal electric field  $c\mathbf{E} = -\mathbf{V} \times \mathbf{B}$ , then the helicity flux rate given by Equation (7), splits into two terms (Berger 1984):

$$\left( \frac{dH_R}{dt} \right) = \underbrace{-2 \int (\mathbf{A}^P \cdot \mathbf{V}_h) B_z da}_{\text{shearing, FI}} + \underbrace{2 \int (\mathbf{A}^P \cdot \mathbf{B}_h) V_z da}_{\text{emergence, DI}}. \quad (8)$$

DFI

The first term corresponds to magnetic helicity generated by flux tubes moving horizontally in the photosphere (shearing), and the second term corresponds to helicity injection due to emergence from the solar interior into the corona. For observations near disk center, where the line-of-sight direction approximates the vertical direction, in Equation (8), we can make the assumption that  $\mathbf{V}_h$  can be determined with our FLCT flow estimates, and

$V_z$  from our Doppler velocity measurements. Adopting the naming convention from §2.3.4 in Kazachenko et al. (2014), shearing and emergence terms would correspond to the FI (**F**ourier **I**deal) and DI (**D**oppler **I**deal) electric-field solutions, respectively, and their sum to the DFI solution (**D**oppler **F**ourier **I**deal). When using the PDFI electric field form of the relative helicity flux (Equation (7)), the shearing and emergence terms are not neatly separated.

When comparing helicity fluxes calculated using the PDFI and DFI techniques, it is important to remember that PDFI and DFI methods are independent of each other, hence their results are not necessarily consistent. For more details on PDFI and DFI helicity fluxes and the quality of their reconstruction using ANMHD simulations, see §3.2 in Kazachenko et al. (2014).

### 3. DATA REDUCTION: AR 11158

We derive the evolution of the magnetic field, electric field, Poynting, and helicity fluxes in NOAA 11158 using series of HMI vector magnetograms and the PDFI method. A six-day, uninterrupted, 12-minute-cadence data set allowed us to study in detail both long-term, gradual evolution, as well as rapid changes centered around the region’s X-class flare. In this section we describe the data set and the coordinate system re-projection we use.

NOAA AR 11158 was the source of an X2.2 flare on 2011/02/15, starting at 01:44 UT, peaking at 01:56 UT, and ending at 02:06 UT. A front-side halo CME accompanied the flare (Schrijver et al. 2011). Prior to the X2.2 flare, the largest flare in this region was an M6.6 on 2011/02/13 at 17:28 UT, a little more than 30 hours before the X2.2 flare.

HMI observed AR 11158 in great detail, routinely generating filtergrams in six polarization states at six wavelengths on the Fe I 617.3 nm spectral line. From these filtergrams, images for the Stokes parameters, I, Q, U, and V were derived which, using the Very Fast Inversion of the Stokes Algorithm (VFISV) code (Borrero et al. 2011), were inverted into the magnetic field vector components. To resolve the  $180^\circ$  azimuthal field ambiguity the “minimum energy” method (Metcalf et al. 1994; Leka et al. 2009) was used. In addition, we flipped the azimuths of the transverse magnetic field vectors in all pixels which exhibited single-frame fluctuations in azimuth of larger than  $120^\circ$  and for which such flipping reduced time variation in the azimuth (Welsch et al. 2013).

#### 3.1. Deriving Magnetic Vector Fields: B

To study pre-flare photospheric magnetic evolution, and to baseline this evolution against post-flare evolution, we obtained 153 hours of 12-minute-cadence  $0.5''$ -pixel HMI

vector-magnetogram data, from the beginning of the active region emergence, about four days before the X2.2 flare, to two days after the flare:  $t_{start}$  = February 10 2011 14:00 UT, with the active region centered at (S19, E50); and  $t_{end}$  = February 16 2011 23:48 UT, with the active region at (S21, W37).

We rotated the active region to disk center and transformed it to a local Cartesian coordinate system (Welsch et al. 2013). To do so, in the first step, we re-projected the observed magnetic vectors’ components onto radial/horizontal coordinate axes. We then converted the Cartesian output grid’s points into plane-of-sky (POS) coordinates, and interpolated the radial and horizontal components of the magnetic field,  $B_r$  and  $\mathbf{B}_h$ , onto the remapped output grid points. Finally, to account for small, whole-frame shifts of the AR’s structure between successive measurements, we co-aligned the data to sub-pixel scale.

The data preparation included a re-projection of the magnetogram surface, from the spherical photosphere to a regular, Cartesian grid. Since FLCT (Fisher and Welsch 2008), and indeed any method of estimating the optical flow (e.g., Schuck (2006)), depends upon image structure (e.g., gradients), conformal mappings are preferred, since they are shape-preserving. Accordingly, we use Mercator re-projection (Welsch et al. 2009), with equally spaced grid points as an input for FLCT. After re-projection, to preserve physical quantities of magnetic fields and velocities, we corrected the fluxes for the distortion of pixel scale introduced by re-projection; the details of the applied correction-factors are given in Appendix A.

For the minimum magnetic field to consider in the PTD, we chose a threshold of  $|\mathbf{B}| = 250$  gauss, consistent with the upper limit of the uncertainty in the horizontal and vertical components of the magnetic field (Hoeksema et al. 2014). To avoid spurious signals in electric fields, we apply a mask, where we set any pixel’s magnetic field components to zero if in any of three consecutive frames it has  $|\mathbf{B}| < 250$  Gauss. To increase the accuracy

of the calculated electric fields we also added a boundary area of 55-pixels width/height padded with zeroes around the periphery of the magnetogram (see §2.1 of Kazachenko et al. (2014)). The final data cube, after re-projection and boundary adding, consists of 770 time steps ( $dt = 720$  sec) and has a field of view of  $665 \times 645$  pixels with a pixel size of 360.16 km, which at disk center is equivalent to the original  $0.5''$  size of HMI's pixels. More details on the data cube preparation and calibration, for a shorter time period, can be found in Welsch et al. (2013).

Figure 1 shows the final vertical magnetic field in a subregion of the full-disk data array after re-projection in the beginning (Panel *A*), middle (*B, C*) and the post-flare (*D*) times of the magnetogram sequence. Note that the positive and negative vertical magnetic fluxes,  $B_z(t)$ , shown on the right panel, nearly balance each other; the magnetic flux increases from essentially zero to roughly  $1.4 \times 10^{22}$  Mx at the time of the flare (vertical dashed line). The flux emerges in two phases – an initial, gradual phase is followed by a much more rapid phase, a pattern seen in the emergence of many active regions (Fu and Welsch 2015).

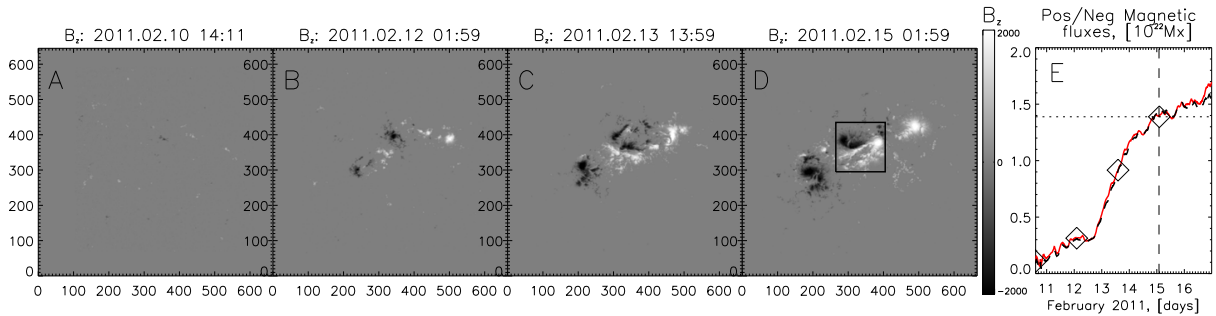


Fig. 1.— *Panels A-D*: HMI vertical magnetic field ( $B_z$ ) maps at 4 different times of AR 11158 evolution. *Panel E*: evolution of the positive and negative vertical magnetic fluxes of the 6-day interval, with the diamonds indicating the times of the four images (A-D) on the left. An X-class flare occurred at the time corresponding to the vertical dashed line. The black box in *Panel D* indicates the field of view of Figures 4–8.

### 3.2. Deriving Velocity Vector Fields: $\mathbf{V}$

To derive the three-component velocity vector of the magnetized plasma, we used the following two methods: the method of Welsch et al. (2013) for calibrated line-of-sight (LOS) Doppler velocity component  $V_{LOS}$ , and FLCT for the horizontal velocities  $V_h$ . To derive and calibrate the Doppler velocity, we used three successive vector magnetograms and one Dopplergram coincident with the central magnetogram. Following the idea of Welsch et al. (2013), that the Doppler shifts measured along polarity inversion lines (PILs) of the LOS magnetic field determine one component of the velocity perpendicular to the magnetic field, we calibrated the quantity  $V_{LOS}$  by subtracting the median Doppler velocity among all pixels on LOS PILs. To find the horizontal velocity  $V_h$ , we determined local displacements of magnetic flux between two successive images in the neighborhood of each pixel, employing the following three steps. First, we masked the initial and final images with a Gaussian windowing function with an  $e$ -folding width of  $\sigma_{FLCT} = 5$  pixels; second, we cross-correlated the two masked images; finally, we found the peak of the cross correlation function. The vector displacement of this peak from zero is the inferred spatial displacement of the pattern in the neighborhood of the windowing function’s center.

To calculate electric fields, and hence helicity fluxes, we use Doppler and FLCT velocities as an input into the PDFI inversion. For comparison, apart from the PDFI, we also use Doppler and FLCT velocities on their own as an independent estimate for the helicity flux rate (see Equation (8)).

To summarize, as a result of the data reduction we obtained a six-day data cube consisting of 768 frames (two frames less than the original dataset to obtain FLCT velocities), each of which contains data for three components of the velocity field and three components of the magnetic field with a field of view of  $665 \times 645$  pixels, a pixel size of 360.16 km, and a time step of  $dt = 720$  sec.

### 3.3. How do Errors in Magnetic Field Measurements Affect our Electric Fields?

When testing the PDFI electric field inversion technique using MHD simulations (Kazachenko et al. 2014), we have the advantage of knowing that the errors in the input data are zero, but such is not the case with the HMI data (Liu et al. 2012b). Hence to estimate the uncertainties in the derived electric field and Poynting fluxes, we have to account for uncertainties in the input HMI input data, which arise primarily from estimation and inversion of the Stokes profiles (Liu et al. 2012b; Hoeksema et al. 2014).

Assuming that the width of the gaussian fitted to the core of each magnetic field values distribution in the weak-field regions indicates the noise level in the measurements, we estimate the errors in  $B_x$ ,  $B_y$  and  $B_z$  in AR 11158 dataset during six days of AR evolution (see Figure 2). The fluctuation of the error in  $B_x$ ,  $B_y$  and  $B_z$  varies within 100 Gauss for the horizontal magnetic field and within 30 Gauss for vertical magnetic field due largely to effects arising from SDO’s 24-hr. orbital period. We use those values, i.e., [100, 100, 30] gauss, respectively, as noise thresholds for magnetic field values.

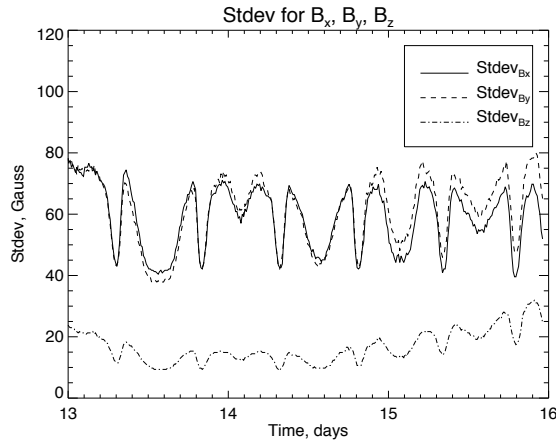


Fig. 2.— Estimated noise levels in  $B_x$ ,  $B_y$  and  $B_z$ , as functions of time in February 2011. Note the periodic variation, believed to be a function of orbital phase of the SDO satellite.



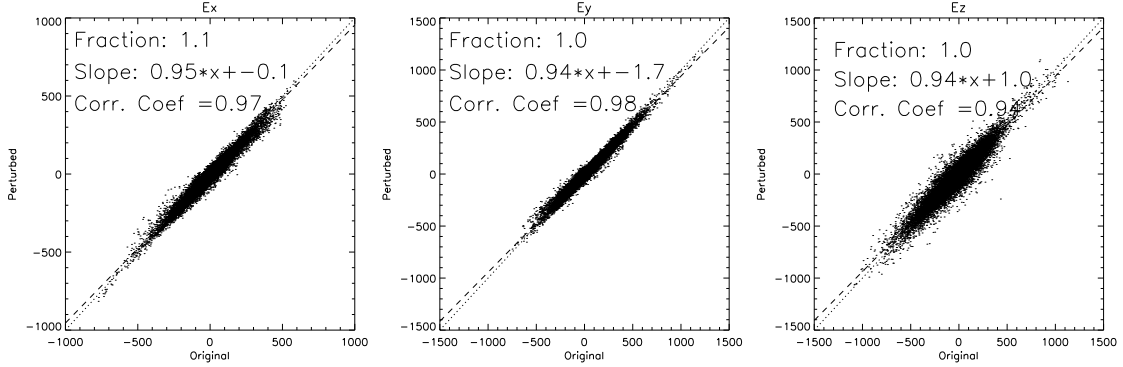


Fig. 3.— Pixel-by-pixel scatter plots showing the ensemble of perturbed electric field solutions as a function of the unperturbed electric field solution, for all three components of  $\mathbf{E}$ , for one particular realization of pseudo-random noise.

We use Monte Carlo simulations to estimate the errors in the PDFI electric fields caused by the uncertainty in the HMI data. The sensitivity of PDFI electric field solutions to vector magnetogram noise is exacerbated by the fact that source terms of the Poisson equations that are solved as part of the electric field inversions involve temporal and/or spatial derivatives, which greatly amplify the noise. This is, however, ameliorated by the fact that solutions to Poisson’s equation tend to smooth out the effect of noisy source terms. Since the entire inversion procedure is quite complex, our approach is to start from a given set of input magnetic field data, and then add pseudo-random, Gaussian perturbations to the data, consistent with the noise thresholds given above ( $[100, 100, 30]$  gauss). By comparing the ensemble of electric field solutions that are perturbed about our initial solution, we can characterize the resulting errors of the electric field inversion. Figure 3 shows three scatter plots between the original and the perturbed the electric fields for one particular realization of pseudo-random noise, one plot for each component.

The resulting uncertainties in  $E_x$  and  $E_y$  are smaller than those for  $E_z$ , reflecting the fact that the inductive horizontal electric field from PTD,  $\mathbf{E}_h^P$ , depends on  $B_z$ , which has

much smaller intrinsic errors than  $B_x$  and  $B_y$ , while the inductive part of the vertical electric field,  $E_z^P$ , depends on the more-noisy  $B_x$  and  $B_y$ . Thus our study not only shows that the electric field inversion errors are not too large, but the distribution of these errors about the diagonal line provides quantitative estimates for the random errors, and deviations from unit slope provide some information about more systematic errors. To scale the deviations relative to the unperturbed electric fields, we fit the difference between the electric field from the perturbed magnetic field and the electric field from the unperturbed magnetic field with a Gaussian and then normalize it by dividing it by the standard deviation of the unperturbed data. We find that the standard deviation  $\sigma = [0.14, 0.13, 0.18, 0.14]$  for  $E_x$ ,  $E_y$ ,  $E_z$  and  $S_z$ , respectively.

To summarize, the levels of the errors in the HMI data lead to errors in the electric field up to 14% and 13% in  $E_x$  and  $E_y$  and 18% in  $E_z$ . The error in the vertical Poynting flux,  $S_z$ , is 14%. If we add these uncertainties from the data (in quadrature) to the errors in the total Poynting flux that we found when testing the PDFI method (where the discrepancy,  $\delta S_z$ , ranged from 1% to 25% for viewing angles ranging from 0 to 60°, see Figure 10 of Kazachenko et al. (2014)), then we end up with the error ranging from 14% to 29% in the vertical Poynting flux.

## 4. RESULTS

To describe the photospheric electric fields  $\mathbf{E}$  and energy fluxes  $\mathbf{S}$  in evolving AR 11158, we use two approaches. In Section 4.1 we show the spatial distribution of  $\mathbf{B}$ ,  $\mathbf{V}$ ,  $\mathbf{E}$  and  $\mathbf{S}$  at two times, before and after the X2.2 flare. In Section 4.2 we analyze their temporal spatially integrated evolution over the six days of observation. These approaches allow us to capture both the spatial structure at quiet times before the flare with the change that the flare causes, and the overall long-term behavior of the active region.

### 4.1. Properties Of the Active Region AR 11158 Before and After the X2.2 Flare

As an example of the spatial distribution of electric fields and Poynting fluxes in AR 11158, we selected two moments before  $T_{pre} = 01 : 36$  UT and after  $T_{post} = 02 : 12$  UT the X2.2 flare. These moments are of particular interest since the photospheric vector magnetic field changed abruptly during the flare (Petrie 2012; Wang et al. 2014), and different flare signatures, such as flare ribbons, have been observed during this time frame. Here we investigate the changes in velocities, electric fields, and Poynting fluxes associated with these changes. We note that the 12-minute-cadence data shown here are derived from a tapered temporal average that is performed every 720 seconds using observations collected over 22.5 minutes (1350 s) to reduce noise and minimize the effects of solar oscillations.

#### 4.1.1. Magnetic Field: $\mathbf{B}_{pre}$ and $\mathbf{B}_{post}$

Figure 4 shows the vector magnetic fields  $\mathbf{B}$  centered at NOAA 11158 before (pre-flare,  $T_{pre} = 01 : 36$  UT) and near the end of the flare (post-,  $T_{post} = 02 : 12$  UT) and also the difference image between the two (right panel). As seen from the right panel, the horizontal

magnetic field close to PIL increased by over 300 G during the flare (see arrows), while the vertical magnetic field remained almost nearly constant. This horizontal-field increase is consistent with magnetic field contraction scenario by Hudson et al. (2008) and is in detail described by Petrie (2012); Wang et al. (2014) and Sun et al. (2012). We notice the two circular patterns, directed counter-clockwise in negative and clockwise in positive polarities – direct evidence of an abrupt magnetic twist decrease in both sunspots during the flare, which clearly contradicts arguments (by, e.g., Melrose 1995) that the vertical electric current density through the photosphere should not change on the flare timescale. The sudden change in twist might arise from removal of magnetic helicity from the active-region’s magnetic field by a coronal mass ejection (Longcope and Welsch 2000; Petrie 2012).

#### 4.1.2. *Velocity Field: $\mathbf{V}_{\text{pre}}$ and $\mathbf{V}_{\text{post}}$*

For completeness, in Figure 5 we show the three components of the velocity field at the times before and after the flare as well as the difference image between the two. The Doppler velocity has a strong ( $1 \text{ km s}^{-1}$ ) upflow close to PIL and in the sunspot’s umbra. During the flare the Doppler speed does not exhibit any prominent changes (see the background of the right panel), although such changes have been reported in other flares (Deng et al. 2006). However the horizontal velocity field does change: there is an apparent  $\sim 0.2 \text{ km/s}$  drift of magnetic field away from the PIL during the flare. More details of the horizontal velocity pattern during the flare can be found in Wang et al. (2014), where 45-second cadence HMI intensity maps were used.

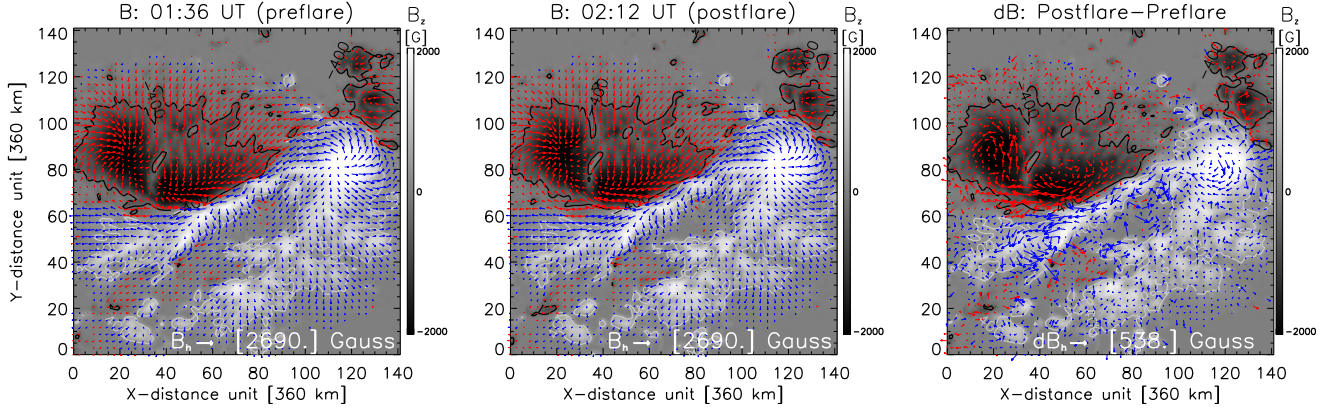


Fig. 4.— Horizontal (arrows) and vertical (grayscale background) components of the magnetic field in NOAA 11158 at pre-flare (*left*) and post-flare times (*middle*), and the difference horizontal field between the two, post- minus pre-flare (*right* panel). The background white and black colors represent positive and negative vertical magnetic fields, respectively. The blue and red colors correspond to horizontal field in areas of positive and negative values of the background vertical magnetic field  $B_z$ . The white and black contours outline the positive and negative vertical magnetic fields at  $B_z = \pm 400$  gauss. The arrows in the right bottom corners show scales for horizontal magnetic field vectors,  $\mathbf{B}_h$  (left and middle panels) or its change,  $d\mathbf{B}_h$  (right panel).

#### 4.1.3. Electric Field: $\mathbf{E}_{\text{pre}}$ and $\mathbf{E}_{\text{post}}$

Finally, in Figure 6 we show the vector electric field maps (“vector electrograms”) calculated using the PDFI method before and after the flare, and the difference between the two. The black island at the PIL before and after the flare reflects a presence of the strong vertical electric field of 1.5 V/cm at the PIL directed into the Sun that remains nearly constant during the flare. What are the physical consequences of the presence of a strong vertical electric field? The spatial distribution of the vertical component of the inductive electric field from PTD,  $E_z^P$ , is related to the time derivative of vertical current density via  $\partial_t J_z = c(\nabla^2 c E_z^P)/(4\pi)$ . Hence, the presence of a nonzero  $E_z$  is related to changes in the

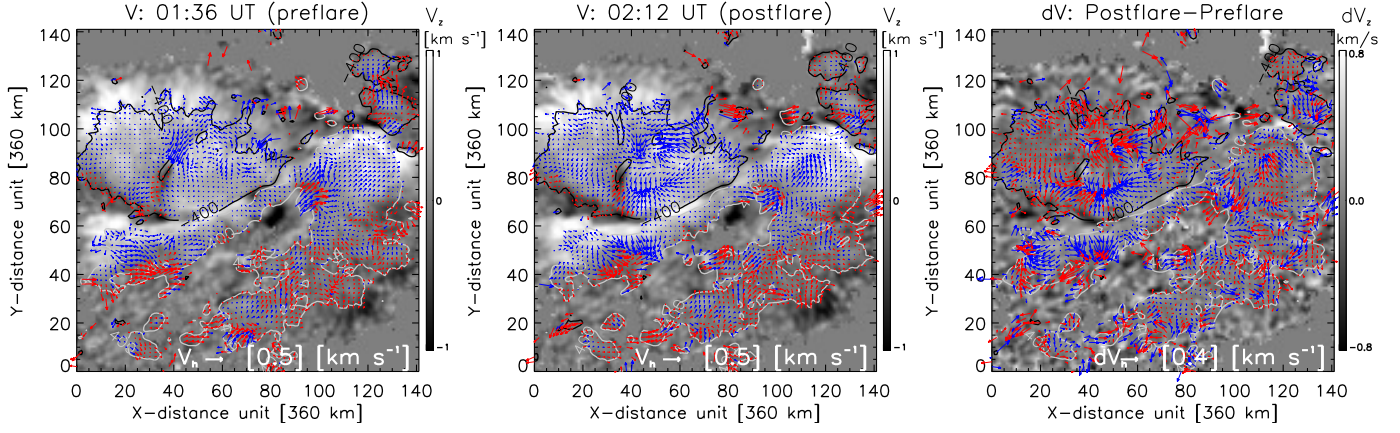


Fig. 5.— Horizontal (arrows) and vertical (background) velocity field in NOAA 11158 at pre-flare (*left*) and post-flare times (*middle*), and the difference image between the two (*right*). The background white and black colors represent positive and negative Doppler velocities, respectively, where positive is toward the viewer (opposite the usual astrophysical convention). The blue and red colors correspond to  $\mathbf{V}_h$  originating in areas of positive and negative values of background vertical velocity. The white and black contours outline the positive and negative vertical magnetic fields at the 400 gauss level. The arrows in the right bottom corners show scales for horizontal velocities.

vertical current, which is mostly concentrated close to the main PIL (Petrie 2013; Janvier et al. 2014). In addition, in the presence of steady upflows at the PIL, the large horizontal magnetic field that points along the PIL there implies that a non-inductive, horizontal electric field,  $\mathbf{E}_h^D$  — the “D” in PDFI — runs across the PIL. Given the flare-driven increase in the horizontal magnetic field at and near the flaring PIL, this  $\mathbf{E}_h^D$  also increases, by up to 0.5 V/cm, as shown in Figure 6.

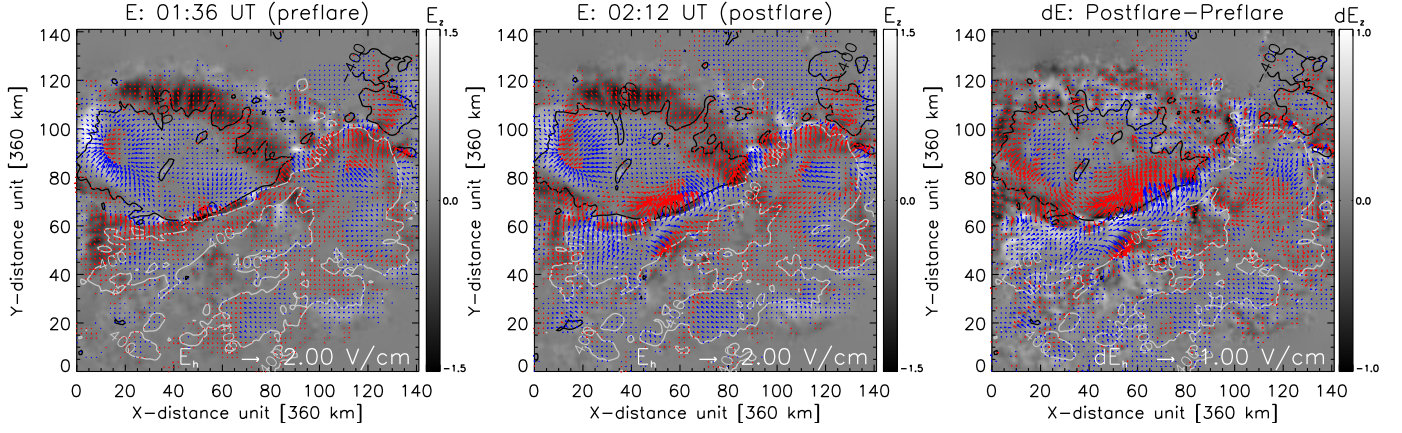


Fig. 6.— “Electrogram”: Horizontal (arrows) and vertical (background) electric field components in NOAA 11158 at pre-flare and post-flare times, and the difference image between the two. The blue and red colors correspond to  $\mathbf{E}_h$  in areas of positive and negative background  $E_z$ . The white and black contours outline the positive and negative vertical magnetic fields at 400 gauss level. The arrows in the right bottom corners show scales of horizontal vectors.

#### 4.1.4. Poynting Flux Vector: $\mathbf{S}_{pre}$ and $\mathbf{S}_{post}$

Figure 7 shows snapshots of the three components of the Poynting flux vector,  $\mathbf{S} = \frac{c}{4\pi} \mathbf{E} \times \mathbf{B}$ , before and after the flare and also the difference image between the two. The range of the vertical Poynting flux shown on the color table is  $[-1, 1] \times 10^{10} \text{ ergs} \cdot \text{cm}^{-2} \cdot \text{s}^{-1}$ . The maximum value of this range is six times smaller than the steady-state photospheric energy flux estimated from the Stefan-Boltzmann law,  $f \sim 6 \times 10^{10} \text{ erg} \cdot \text{cm}^{-2} \cdot \text{s}^{-1}$ . If we look at the typical mean values of the  $S_z$  across the box, shown on the right panel of Figure 7, then we find even smaller absolute values, ranging from  $10^8$  to  $10^9 \text{ ergs} \cdot \text{cm}^{-2} \cdot \text{s}^{-1}$ . The strongest vertical Poynting fluxes are found close to the main PIL: during the flare their mean positive (negative) values within a box on the right panel change from 1.8 (−0.6) to 4.5 (−1.4)  $10^9 \text{ ergs} \cdot \text{cm}^{-2} \cdot \text{s}^{-1}$  respectively, or in terms of total energy flux injected close to PIL, from  $1.3 \times 10^{27}$  to  $4.9 \times 10^{27} \text{ ergs s}^{-1}$  (see white enhancement on the right panel).



Summed over the 22 minutes of the GOES flare time for this event, such an energy flux would amount to about  $4.1 \times 10^{30}$  erg — a small fraction of the  $10^{32}$  erg (or more) released in a large flare such as this.

Similar to the evolution in  $E_h$ , the magnitude of the horizontal component of the Poynting flux,  $S_h$ , increases near the PIL by up to  $8 \times 10^9$  ergs  $\cdot$  cm $^{-2}$   $\cdot$  s $^{-1}$ . As noted above, the combination of steady upflows found in the Dopplergrams at and near the PIL with the systematic increase in the transverse magnetic fields along the PIL leads to an increase in the non-inductive, horizontal electric field,  $\mathbf{E}_h^D$ , which in turn produces an increase in the vertical Poynting flux there.

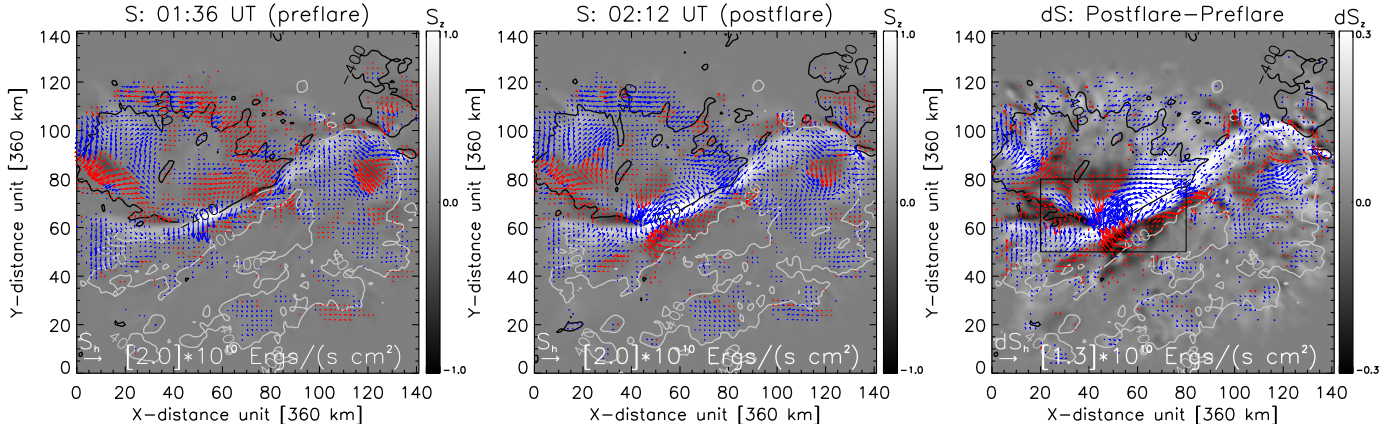


Fig. 7.— Horizontal (arrows) and vertical (background) Poynting vector field components in NOAA 11158 at pre-flare and post-flare times, and the difference image between the two. The blue and red colors correspond to  $\mathbf{S}_h$  in positive and negative areas of the background  $S_z$ . The white and black contours outline the positive and negative vertical magnetic fields at 400G. The arrows in the right bottom corners show scales of horizontal vectors. The range of the background  $S_z$  is  $[-1, 1] \times 10^{10}$  ergs cm $^{-2}$  s $^{-1}$  in the left two panels and  $[-0.3, 0.3] \times 10^{10}$  erg cm $^{-2}$  s $^{-1}$  in the right panel.

Summarizing some of the changes in the photosphere during the flare, in Figure 8, we show the vertical and horizontal magnetic fields, horizontal electric field and the vertical



Poynting flux before and after the flare and also the scans along a fixed  $x$  value (or column in the 2D image) through the center of the active region across the PIL at those two moments (right column). As mentioned above, while the vertical magnetic field does not exhibit any significant changes, the horizontal magnetic field increases at the PIL by several hundred gauss (see  $B_h$ -panel, right column). This leads to an increase in the horizontal Doppler electric field close to PIL by up to 0.5 V/cm and by almost 1 V/cm in some locations away from the PIL (see middle dotted line of the  $E_h$ -panel, right column) and an increase in the vertical Poynting flux from  $1.25$  to  $2.25 \times 10^9$  ergs·cm<sup>-2</sup>s<sup>-1</sup>, i.e. by  $10^9$  ergs·cm<sup>-2</sup>s<sup>-1</sup>.

## 4.2. Six-Day Evolution of Vertical Energy and Helicity Fluxes

To quantify the long-term evolution of the energy and helicity fluxes in AR 11158, we integrate the photospheric Poynting and helicity flux maps over the AR’s field of view ( $665 \times 645$ -pixels) and analyze their behavior over 6 days (768 time steps).

### 4.2.1. Evolution of Free, Potential, and Total Poynting Fluxes

Panels (A-F) of Figure 9 show the six-day time evolution of area-integrated vertical Poynting flux and the potential and free vertical energy fluxes:  $[S_{z,p}, S_{z,f}, S_z]$ . The potential component,  $S_{z,p}$  is calculated by taking a time derivative of the coronal potential energy, computed as a surface integral over the photosphere, with the potential function computed using a Green’s function technique. The free component is the difference between  $S_z$  and  $S_{z,p}$ . In the three insets on the left panels we also show evolution in  $S_z$  from one hour before to four hours after the flare. In panels A and C, large fluctuations are present in  $S_{z,p}$  and  $S_z$  (which were calculated independently), with timescales ranging from about 4 – 24 hr.

In panel B,  $S_{z,f}$  does not exhibit such strong fluctuations at shorter timescales, which evidently cancel out in the difference  $S_z - S_{z,p}$ ; a residual 24-hr. periodicity can still be seen, though. These fluctuations are related to orbital motions of the SDO satellite (Liu et al. 2012b) and are present over the whole field of view. Unfortunately, these fluctuations are internal to the HMI polarization measurements, hence their removal is a time-consuming and complicated task. Efforts to address these artifacts are underway, but they have not been fully addressed. Fortunately, when these fluctuations are integrated over several hours, they do not cause large fluctuations in the total cumulative fluxes (see panel E).

How do  $S_{z,p}$ ,  $S_{z,f}$ , and  $S_z$  change during the flare? Insets of Panels A-C of Figure 9 show that  $S_{z,f}$  and  $S_z$  increase during the flare, after which they return to nearly pre-flare values. We explain this change in the following way. Since the change in the magnetic field close to the PIL is practically a step function (Petrie 2012), the value of the Poynting flux, which involves the temporal derivative of magnetic field, should indeed appear like a delta function. We conclude that while the transients in the vertical Poynting flux include spurious signals due to flare-induced effects on the HMI spectral line (Maurya et al. 2012), the observed peak in the Poynting flux around the flare time is real. (The spatial distributions of the Poynting flux before and after the flare are shown in the bottom row of Figure 8.)

Panel D shows a steady growth in the region’s total unsigned flux after 14 Feb, after the bulk of the region’s flux has emerged. The growth at the time of the flare is consistent with the steady upflows seen along the main PIL, which we expect carry magnetic fields upward from the solar interior, across the photosphere. A slight 24-hr periodicity is discernible from 14 February onward.

As shown in panel E, if we integrate  $S_{z,f}$ ,  $S_{z,p}$  and  $S_z$  in time, the fluctuations seen in panels A-C largely disappear. Notably, no contribution from the flare transient is obvious.

We also observe that, for a time, in the early evolution of the active region, it appears to possess negative free energy, a spurious result. A probable explanation for this is that our Poynting flux estimates systematically underestimate the true energy flux; since the potential field estimate only depends upon  $B_z$ , it does not suffer from this systematic error. To conclude, taking our results at face value, we find the total energy input through the photosphere in five days by the flare time to be  $E = 10.6 \times 10^{32}$  erg, which consists of  $E_p = 8.6 \times 10^{32}$  erg of potential energy and  $E_f = 2.0 \times 10^{32}$  erg of free energy. If instead of computing the potential field using just the Neumann boundary condition, given by  $B_z$ , we had used a “hybrid” Dirichlet-Neumann boundary condition (Welsch and Fisher 2015), which uses both  $(\nabla_h \cdot \mathbf{B}_h)$  and  $B_z$  from the HMI data, our estimate of the potential energy would be  $E_p = 4.2 \times 10^{32}$  implying three times more free energy  $E_f = 6.4 \times 10^{32}$  erg. (This alternative approach might also ameliorate the negative free energy found in the early part of the active region’s development.)

#### 4.2.2. Helicity Flux Evolution

Figure 10 shows time evolution of area integrated helicity flux rates  $\frac{dH_R}{dt}$  (top row) and helicity fluxes  $H_R$  (bottom row) in NOAA 11158. Left panels show  $\frac{dH_R}{dt}$  and  $H_R$ , calculated with the DFI technique, and their components due to shearing (FI) and emergence (DI). Right panels compare  $\frac{dH_R}{dt}$  and  $H_R$  from DFI and PDFI electric fields. (For more information about our naming convention, see Table 1 in Kazachenko et al. (2014)). First, we notice that the emergence term, DI, exhibits much larger fluctuations than shearing term (top left). The apparent large-scale 24-hour periodicity is probably due to signal contamination from the satellite motion (Liu et al. 2012b). If we integrate both curves over time (bottom left), the accumulated helicity flux from shearing dominates the total helicity flux before the flare, consistent with the conclusion by Liu and Schuck (2012). Second, we find that

the helicity flux rates from both DFI and PDFI reach their approximate maximum value at the flare time, consistent with Figure 12 of Liu and Schuck (2012). If we compare helicity fluxes calculated from the PDFI electric fields (PDFI) and the velocity field alone (DFI) (top right), we find that until 12:00 UT on February 14 2011, the two helicity flux rates match each other. At later times, however, they diverge:  $\frac{dH_R}{dt}$  from the velocity field (DFI) becomes significantly larger than that from the PDFI electric field. Note that the primary extra input to the PDFI results compared to DFI results is information about  $\dot{J}_z$ , which sets the inductive  $E_z$ ; this, in turn, is coupled to  $\mathbf{E}_h$  through the ideal Ohm’s constraint,  $\mathbf{E} \cdot \mathbf{B} = 0$ . To investigate the role that the ideal Ohm’s constraint plays in the PDFI helicity estimate, we calculate the helicity flux rate using the PDF (i.e. PTD-Doppler-FLCT) electric fields. We find that the PDF and the DFI helicity flux rates have a similar time evolution, although the PDF helicity flux rate is somewhat smaller than the DFI rate. The discrepancy between PDFI and DFI helicity flux rates could arise because the DFI helicity flux rate is only sensitive to emergence and shearing. Shearing motions however, can then induce the photospheric field to unwind via the propagation of torsional Alfvén waves into the interior, along with the accompanying  $\dot{J}_z$  and  $E_z$  signatures, that only PDFI captures (cf., the transient twist variations modeled by Longcope and Welsch 2000). The constraint  $\mathbf{E} \cdot \mathbf{B} = 0$  then couples the resulting change in  $E_z$  (and  $\dot{J}_z$ ) to a change in  $E_h$ , thereby further reducing the PDFI helicity flux rate.

Integrating over time we find that the total accumulated helicity flux injected through the photosphere during the five days of our magnetogram sequence until the flare time (bottom right) is  $H_{R,DFI} = 7 \times 10^{42} \text{ Mx}^2$ , which is similar to the value from PDFI:  $H_{R,PDFI} = 8.5 \times 10^{42} \text{ Mx}^2$ .

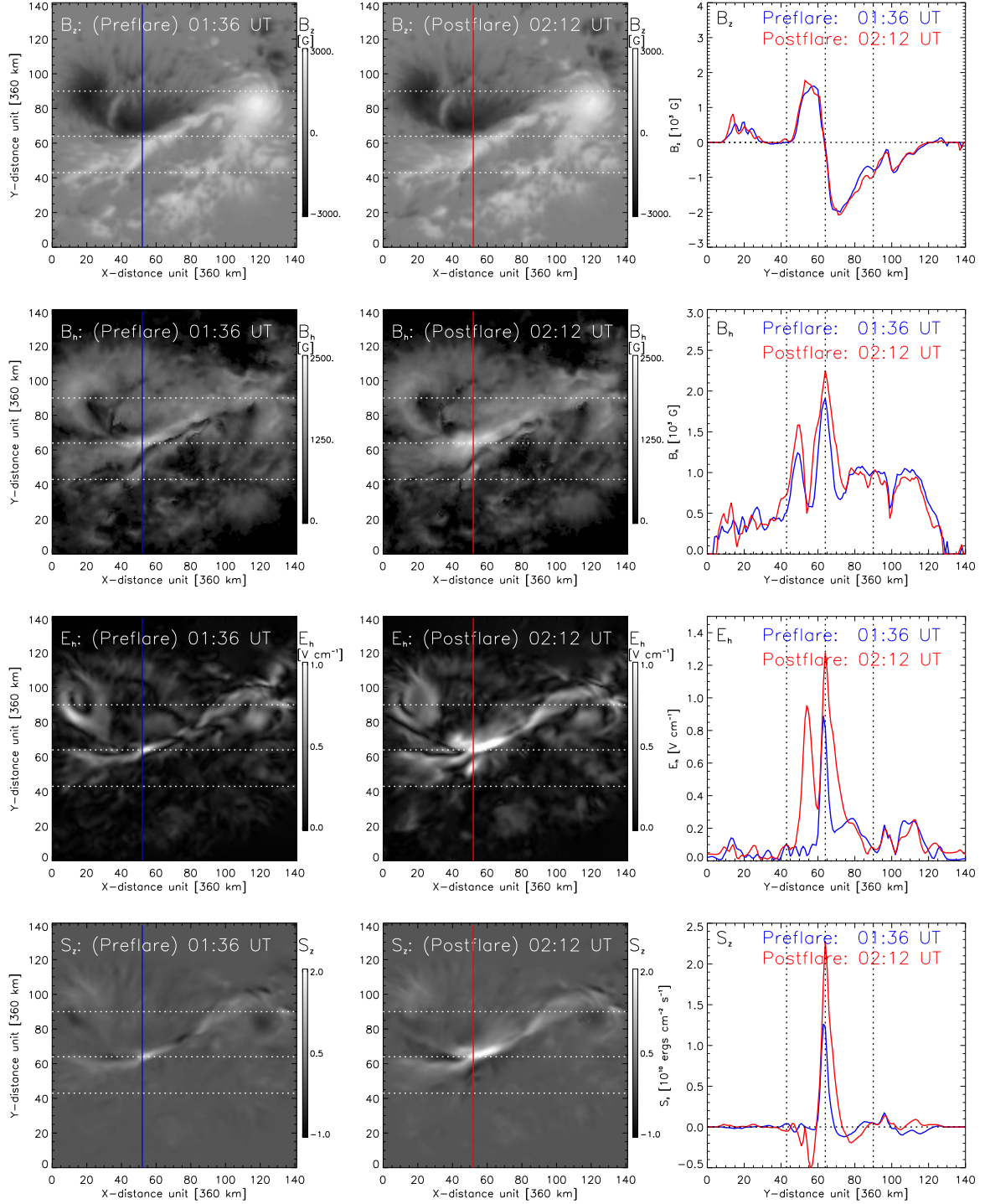


Fig. 8.— *Left and Middle columns:* Vertical and horizontal magnetic fields, horizontal electric field, and the vertical Poynting flux before and after the flare. *Right column:* Vertical scans for  $B_z$ ,  $B_h$ ,  $E_h$  and  $S_z$  before (blue) and after (red) the flare at the locations shown with blue and red lines in the two left columns. Horizontal dotted lines on left and middle panels correspond to vertical dotted lines on the right panel.

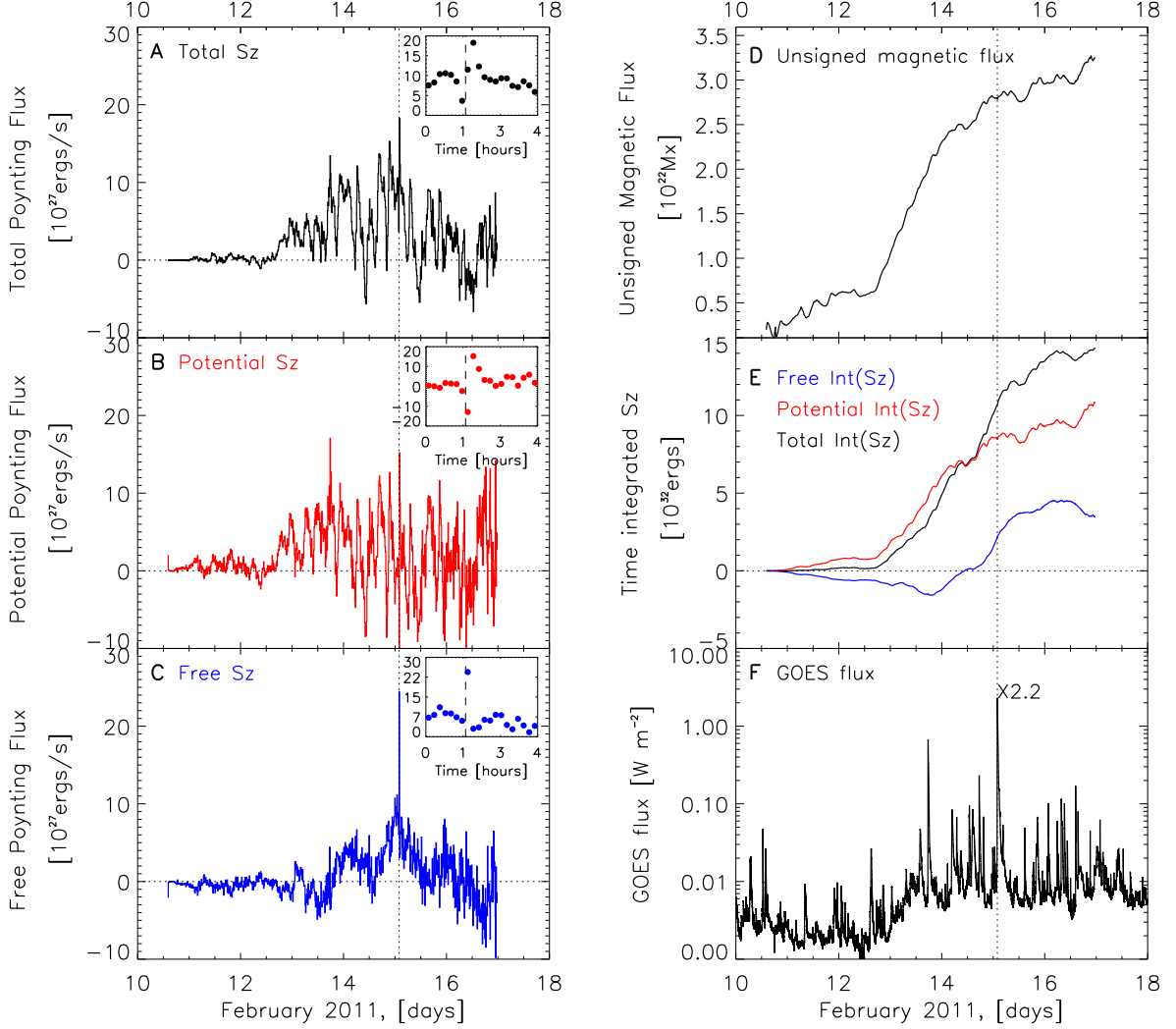


Fig. 9.— Evolution of magnetic and Poynting fluxes in NOAA 11158 during six days: (A-C) Area-integrated potential (A), free (B) and total (C) Poynting fluxes. Corner insets show evolution of the same quantities one hour before and 2 hours after the flare; the X-axis is in hours; (D) Area integrated unsigned magnetic flux, (E) Area and time integrated free and potential components of the vertical Poynting flux and their sum, (F) GOES 5 min soft X-ray light curve (1-8 Å channel). The vertical dotted line indicates the GOES flare peak time at 01:56 UT. All the quantities were calculated within the FOV shown in Figure 1.

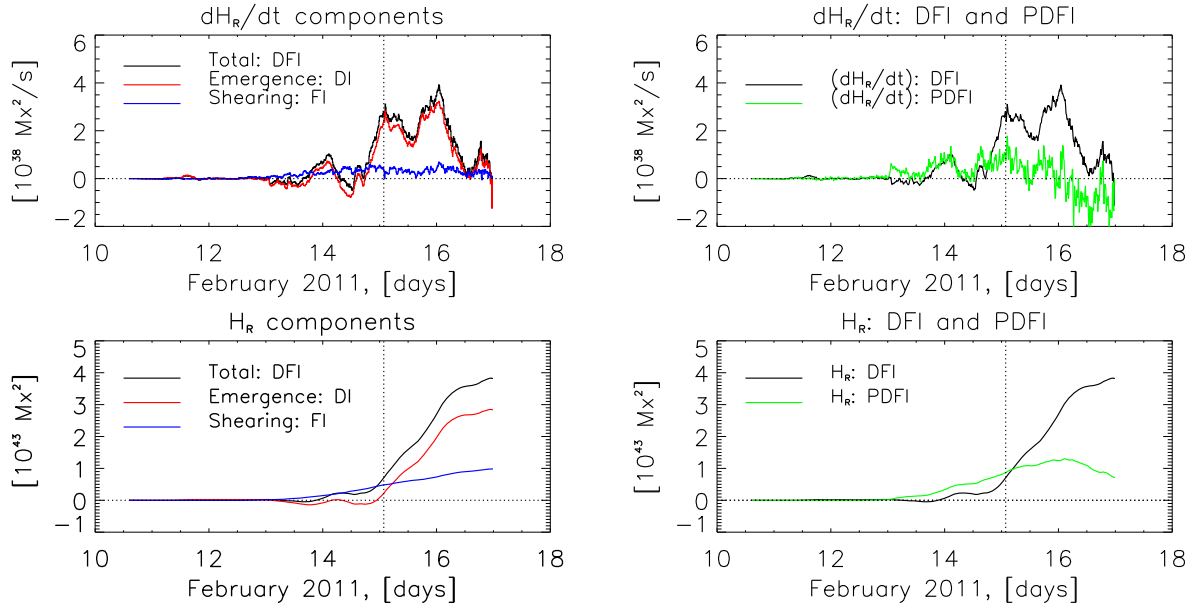


Fig. 10.— *Top Left*: Area integrated helicity flux rate,  $\frac{dH_R}{dt}$  from emergence (red, DI) and shearing (blue, FI), and their sum in NOAA 11158 (black, DFI). *Bottom Left*: Same as above, but integrated in time. *Top Right*: Comparison of area integrated helicity fluxes,  $\frac{dH_R}{dt}$  calculated using velocities (DFI, black) and electric fields (PDFI, green) methods; *Bottom Right*: Same as above, but integrated in time.

## 5. DISCUSSION

Here, we discuss how electric fields, energy fluxes (Poynting fluxes), and helicity fluxes estimated with the PDFI method compare to earlier results.

Using the PDFI method, we find photospheric electric field components in AR 11158 that vary from zero to 1.5 V/cm. While strong horizontal electric fields are present in the whole active region, varying from 0 to 1.2 V/cm, the largest vertical electric field is concentrated mostly near the PIL and the sunspot penumbrae with the maximum values reaching 1.5 V/cm directed inward to the sun. As a result of magnetic field changes during the flare, the horizontal electric field (from the steady upward Doppler flow crossed with the horizontal magnetic field along the PIL) increases by up to 0.4 V/cm perpendicular to the PIL, while the vertical electric field at PIL remains nearly constant  $E_z \approx -1.5$  V/cm.

How do our estimates of the photospheric electric fields compare to results from earlier work? To our knowledge, there have been very few attempts to estimate all three components of the electric field in the photosphere. For example, using LCT, Liu and Zhang (2006) examined only the vertical component of inductive electric field, finding the maximum of  $E_z$  to be  $E_z \approx [0.1 - 0.2]$  V/cm, i.e. significantly smaller than our estimates. Other attempts have focused on estimating the electric field in the corona inside the reconnecting current sheet (RCS) (Poletto and Kopp 1986; Wang et al. 2003, 2004; Qiu et al. 2002, 2004; Jing et al. 2005). For example, using a relationship between the electric field along the current sheet and the observable velocity and magnetic field (Priest and Forbes 2000), Poletto and Kopp (1986) derived the maximum value of electric field in the RCS to be 2 V/cm. In a similar way, Wang et al. (2003) found the coronal electric field during the two-ribbon flare occurring in two stages: the coronal electric field remained near 1 V/cm averaged over 20 minutes during the first stage, and was followed by values of 0.1 V/cm over the next 2 hours. Finally, in one of the latest studies on the subject, Jing et al.



(2005) analyzed a sample of 13 two-ribbon flares, and found the maximum electric field inside the RCS to be in the range of  $0.2 - 5$  V/cm. To summarize the above, all electric fields estimated inside the reconnecting current sheet fall within the range of photospheric electric fields that we find here for AR 11158,  $[0, 5]$  V/cm.

Using the electric and magnetic fields, we estimate the three components of the photospheric Poynting flux vector. We find the amplitude of the maximum Poynting fluxes in the active region to be  $S_z \approx 2 \times 10^{10} \text{ ergs} \cdot \text{cm}^{-2} \text{ s}^{-1}$ , i.e. several times smaller than the steady state solar luminosity,  $6 \times 10^{10} \text{ ergs} \cdot \text{cm}^{-2} \text{ s}^{-1}$ , but of the same order of magnitude. If we look at the typical mean values of  $S_z$  across the AR, we find even smaller values, ranging from  $10^8$  to  $10^9 \text{ ergs} \cdot \text{cm}^{-2} \text{ s}^{-1}$ . A question naturally follows this calculation: Is such a Poynting flux consistent with the amount of magnetic energy stored in the coronal part of the active region? This is the question we address in Table 1.

In Table 1, we compare estimates for coronal energy and helicity for AR 11158 that we derive in this paper with results from other papers. In the first four rows, we show results from Tarr et al. (2013); Liu et al. (2012b); Tziotziou et al. (2013); Vemareddy et al. (2012b), where energy and helicity are found from the evolution of photospheric magnetic fields, by summing the energy and helicity flux rates injected through the photosphere from the beginning of the magnetogram sequence until the moment before the flare. In the last five rows, we show results from Tziotziou et al. (2013); Malanushenko et al. (2014); Sun et al. (2012); Jing et al. (2012) and Aschwanden et al. (2014), where a single preflare vector magnetogram is used to estimate the energy and helicity of the corona. The “Method” column shows the type of method used to find the energy and helicity estimates on the right. In some papers, other methods were used to calculate the potential energy; they are indicated with a letter next to the estimate. In addition, we indicate the type of input data used in the calculations. This helps to explain the difference in results between some papers

that used the same methods, but applied them to different input data, e.g. differences in estimates of the potential field energy,  $E_P$ , by Tarr et al. (2013) and Sun et al. (2012), where  $B_{LOS}$  and  $B_z$  have been used respectively.

The total magnetic energy from different models, shown in Table 1, ranges from  $6 \times 10^{32}$  (Malanushenko et al. 2014) ergs to  $12 \times 10^{32}$  ergs (Tziotziou et al. 2013). We noticed that both NLFFF coronal methods, which use the EUV coronal loops instead of the transverse magnetic field as a constraint for the NLFFF extrapolation (Malanushenko et al. 2014; Aschwanden et al. 2014), derive total energies that are the smallest of all total energy estimates:  $6 \times 10^{32}$  ergs and  $8.6 \times 10^{32}$  ergs respectively. In contrast, the photospheric NLFFF methods, which use a vector magnetogram for extrapolation (Sun et al. 2012; Tziotziou et al. 2013), yield the largest estimates for the total energy:  $10.6 \times 10^{32}$  ergs and  $12 \times 10^{32}$  ergs respectively. The cumulative photospheric methods that derive the total energy by integrating the energy flux, inferred from the photospheric velocity or electric fields (the photospheric estimates), yield total energies in between the two. For example, using the MCC method, Tarr et al. (2013) derive  $E = 8.5 \times 10^{32}$  ergs. Using DAVE4VM approach, Liu et al. (2012b) and Tziotziou et al. (2013) yield similar estimates of  $E = 8.8 \times 10^{32}$  ergs and  $E = 8.0 \times 10^{32}$  ergs, respectively. Finally, in this paper using the PDFI method we find the total energy of  $E = [10.6 \pm 3.0] \times 10^{32}$  ergs. Taking the PDFI and HMI uncertainties into account, we find that the total energy, estimated right before the flare, is consistent with  $E$  from DAVE4VM, MCC and NLFFF and is slightly larger than the coronal NLFFF estimates.

If we look at the temporal evolution of energy  $E$ , we notice that  $E$  derived from the PDFI (Figure 9) is consistent with  $E$  from DAVE4VM (Figure 14 in Liu et al. (2012b)) and NLFFF (Figure 4 in Sun et al. (2012)). In fact, the energy  $E$  from the PDFI and DAVE4VM are almost identical until February 14 18:00, and then start diverging several

hours before the flare. By the end of magnetogram sequence, at 18:00 UT on 16 February, the  $E$  from DAVE4VM and PDFI are  $12 \times 10^{32}$  ergs and  $14 \times 10^{32}$  ergs, respectively. Still, this discrepancy lies within our uncertainty in the total energy estimate. Comparing the temporal evolution of  $E$  from PDFI and NLFFFs, we again find that they are consistent with each other, with less than 15% differences between the two, which is within our uncertainty.

The potential energy from different models, also shown in Table 1, ranges from  $4.8 \times 10^{32}$  ergs (Malanushenko et al. 2014) to  $8.6 \times 10^{32}$  ergs (Green’s function, this paper). Similar to our approach, Sun et al. (2012) use the Green’s function and  $B_z$  to estimate potential energy of  $8.0 \times 10^{32}$  ergs, that, within the HMI uncertainty, is consistent with our estimate. The potential energies calculated by Tarr et al. (2013); Malanushenko et al. (2014); Aschwanden et al. (2014) all use the HMI LOS magnetic field and distinct computational methods, which might be the cause of the difference between the estimates.

The free magnetic energy from different models, also shown in Table 1, ranges from  $1.0 \times 10^{32}$  ergs (Aschwanden et al. 2014) to  $2.9 \times 10^{32}$  ergs (Tarr et al. 2013). Using the MCC model and the flare ribbon locations, which allows one to derive the footprint of the reconnecting magnetic fields, Tarr et al. (2013) find the initial pre-flare free energy in the corona to be  $E_f = 2.9 \times 10^{32}$  ergs, consistent with estimates of Sun et al. (2012) and the results of this paper. Tarr et al. (2013) also find that more than 50% of this energy,  $dE = 1.7 \times 10^{32}$  ergs, is released during the flare. Coronal NLFFF methods (Aschwanden et al. 2014; Malanushenko et al. 2014) find that 60% to 80% of the free energy is released during the flare, but the values of the pre-flare free energy  $E_f$  that they find are roughly factors of two (or more) times smaller than the values from Tarr et al. (2013); Sun et al. (2012), and this paper.

Another important fact one must keep in mind when comparing cumulative free Poynting fluxes and coronal free energies, is that the total Poynting flux only gives us

information about the total energy that entered the corona from the photosphere. What we do not know is how much of this total energy leaves the corona from above into the heliosphere during eruptive flares prior the X2.2 flare. For this reason, our PDFI free energy estimate is the upper limit of the energy available in the corona. To summarize, the free magnetic energy, which we find by summing the flux rate of free energy through the photosphere, is up to two times larger than the free energy estimated from the coronal NLFFF code, and 20 – 30% smaller than free-energy estimates from the MCC model and photospheric NLFFF extrapolations (Tarr et al. 2013; Sun et al. 2012). The temporal evolution of the PDFI free energy is within 20 – 30% of  $E_f(t)$  from the photospheric NLFFF code.

Finally, in the last column of Table 1, we compare the total relative magnetic helicities before the X2.2 flare. The time integrated total helicity flux we find with DFI and PDFI techniques is  $H_{R,DFI} = 7 \times 10^{42} \text{Mx}^2$  and  $H_{R,PDFI} = 8.5 \times 10^{42} \text{Mx}^2$  respectively. The difference between the two is consistent with the results we found for the ANMHD test case, where DFI method reconstructed the total helicity around 10% more accurately than the PDFI method (see Table 3 in Kazachenko et al. (2014)). For comparison, using DAVE4VM, Liu et al. (2012b) and Tziotziou et al. (2013) found that the total amount of helicity injected into corona is  $6.5 \times 10^{42} \text{Mx}^2$  and  $8.5 \times 10^{42} \text{Mx}^2$  respectively. These results are consistent with our PDFI estimate, given the differences between the DAVE4VM and the PDFI accuracies (Kazachenko et al. 2014) – the ratio between the total PDFI- and DAVE4VM-reconstructed helicity fluxes and the actual helicity flux are 0.94 and 1.0 respectively for the ANMHD test case (see Table 4 in Kazachenko et al. (2014)). Using a different velocity reconstruction method, DAVE, Vemareddy et al. (2012b) and Jing et al. (2012) find the total relative helicity of  $6.0 \times 10^{42} \text{Mx}^2$  and  $5.5 \times 10^{42} \text{Mx}^2$  respectively. As shown by Schuck (2008) for the ANMHD test case, combining DAVE flows with ANMHD’s vertical velocity overestimates the total helicity flux by at least 40%, hence the disagreement

between DAVE and PDFI results for AR11158 is not surprising. Finally, using different NLFFF approaches, Tziotziou et al. (2013) and Jing et al. (2012) find  $H_R = 13 \times 10^{42} \text{ Mx}^2$  and  $H_R = 5.2 \times 10^{42} \text{ Mx}^2$  respectively. To summarize, using the PDFI method we find the relative magnetic helicity consistent with DAVE4VM estimates (Liu et al. 2012b; Tziotziou et al. 2013), but very different from (and in between) the NLFFF estimates (Tziotziou et al. 2013; Jing et al. 2012).

## 6. CONCLUSION

The electric field on the Sun plays an important role in transporting energy, heating plasma, and accelerating and transporting charged particles. Estimates of photospheric electric and magnetic field vectors make the estimation of Poynting flux of electromagnetic energy crossing the photosphere and the flux of relative magnetic helicity straightforward. Taking advantage of the newly released high temporal and spatial resolution HMI vector magnetograms, and the recently developed PDFI electric-field inversion method (Kazachenko et al. 2014), we apply the method to a six-day sequence of vector magnetic field measurements of AR 11158, from 10-16 February 2011. From these 12-minute cadence measurements, we derive the evolution of electric fields, the Poynting flux, and the helicity flux. During the interval of study, an X2.2 flare occurred, along with 35 M- and C-class flares.

We analyze the spatial distribution of the derived electric field and Poynting flux maps, their temporal evolution, and changes during the X2.2 flare. We compare derived PDFI electric fields with coronal electric fields, PDFI energies and helicities with NLFFF, MCC and DAVE4VM estimates. The results are the following:

1. We find the photospheric electric field vector, which typically ranges from 0 to 1.5

Table 1: Summary Table: Comparison of coronal energy and helicity in AR 11158 where an X2.2 flare occurred on February 15 2011 01:35 UT:  $dE$  - change in the coronal free magnetic energy during the flare,  $[E_f, E_p, E]$  - free, potential and total magnetic energies in the corona before the flare at 01:35 UT,  $H_R$  – relative magnetic helicity in the corona before the flare at 01:35 UT. In *Photospheric estimates*, coronal energy and helicity are calculated cumulatively, i.e. by integrating photospheric energy and helicity flux rates in time. In *Coronal Estimates* energy and helicity are calculated instantaneously, using extrapolation of the photospheric vector magnetic fields. All quantities have been calculated using the indicated *Method*, unless a more specific method is used, like in the case of potential energies (see letters <sup>(d)</sup>–<sup>(f)</sup>). In photospheric estimates we use a start time of 14:11 UT on 10 February.

Paper	Method	Data	$dE$	$E_f$	$E_p$	$E$	$H_R$
			10 <sup>32</sup> ergs				10 <sup>42</sup> Mx <sup>2</sup>
Photospheric Estimates							
This paper	PDFI Method	<b>B, V<sub>z</sub></b>	–	<b>2.0</b>	<b>8.6<sup>(d)</sup></b>	<b>10.6</b>	<b>8.5</b>
...	DFI method	<b>B, V<sub>z</sub></b>	–	–	–	–	7.8
Tarr et al. (2013)	MCC model	$B_{LOS}$	1.7	2.9	5.6 <sup>(d)</sup>	8.5	–
Liu et al. (2012b)	DAVE4VM	<b>B, V<sub>z</sub></b>	–	–	–	8.8	6.5
Tziotziou et al. (2013)	DAVE4VM	<b>B, V<sub>z</sub></b>	–	–	–	8.0	8.5
Vemareddy et al. (2012b)	DAVE	<b>B</b>	–	–	–	–	6.0
Jing et al. (2012)	DAVE	<b>B</b>	–	–	–	–	5.5
Coronal Estimates							
Malanushenko et al. (2014)	Coronal NLFF <sup>(a)</sup>	$B_{LOS}$	1	1.2	4.8 <sup>(e)</sup>	6	–
Aschwanden et al. (2014)	Coronal NLFF <sup>(a)</sup>	$B_{LOS}$	0.6	1.0	7.6 <sup>(f)</sup>	8.6	–
Sun et al. (2012)	NLFFF method <sup>(b)</sup>	<b>B</b>	0.3	2.6	8.0 <sup>(d)</sup>	10.6	–
Tziotziou et al. (2013)	NLFFF method <sup>(c)</sup>	<b>B</b>	0.8	–	–	12	13
Jing et al. (2012)	NLFFF method <sup>(b)</sup>	<b>B</b>	–	–	–	–	5.2

*NLFFF method:* <sup>(a)</sup> – EUV loops instead of  $B_t$  are used as a constraint, <sup>(b)</sup> – Wiegelmann (2004),

<sup>(c)</sup> – Georgoulis et al. (2012). *Potential field methods:* <sup>(d)</sup> – Green’s function, Sakurai (1989),

<sup>(e)</sup> – Alissandrakis (1981), <sup>(f)</sup> – Aschwanden and Sandman (2010).

V/cm, increases its magnitude by up to 1 V/cm during the flare. The horizontal component is mostly concentrated along the PIL, while the vertical component is largest at the PIL and in the sunspots’ penumbrae. The range of photospheric electric fields is consistent with the coronal electric fields, derived from the flare ribbon’s motion.

2. We find the photospheric Poynting flux ranging from 0 to  $2 \times 10^{10} \text{ erg}\cdot\text{cm}^{-2}\text{s}^{-1}$ , with mean values of  $10^8$  to  $10^9 \text{ erg}\cdot\text{cm}^{-2}\text{s}^{-1}$ . The largest vertical Poynting flux is concentrated at the PIL.
3. Integrating the Poynting flux in time we find the total magnetic energy before the flare,  $E = [10.6 \pm 3.0] \times 10^{32} \text{ ergs}$ . In spite of a very different approach, it is consistent within the uncertainty with the total energies from DAVE4VM, MCC and NLFFF methods’ estimates and larger than the coronal NLFFF estimates.
4. The potential field magnetic energy before the flare, estimated from the Green’s function,  $E_p = 8.6 \times 10^{32} \text{ ergs}$ , is consistent with  $E_p = 8.0 \times 10^{32} \text{ ergs}$  (Sun et al. 2012). Tarr et al. (2013); Malanushenko et al. (2014) and Aschwanden et al. (2014) derive a similar or somewhat smaller  $E_p$ , using  $B_{LOS}$  instead of  $B_z$  and a different computation method.
5. The free magnetic energy before the flare,  $E_f = 2.0 \times 10^{32} \text{ ergs}$ , is up to two times larger than the free energy estimated from the coronal NLFFF code (Aschwanden et al. 2014; Malanushenko et al. 2014), and 20 – 30% smaller than the free energy estimates from MCC model and photospheric NLFFF extrapolations (Tarr et al. 2013; Sun et al. 2012).
6. Analyzing the temporal evolution of cumulative energy,  $E$ , from PDFI, NLFFF and DAVE4VM, we find less than 15% differences between the three. The temporal

evolution of the PDFI  $E_f$  is less than 20 – 30% different from the  $E_f$  from the photospheric NLFFF codes and several times larger than  $E_f$  from the coronal NLFFF codes (Aschwanden et al. 2014).

7. We find the relative magnetic helicity to be consistent with DAVE4VM estimates (Liu et al. 2012b; Tziotziou et al. 2013), but very different from the NLFFF estimates (Tziotziou et al. 2013; Jing et al. 2012).
8. Using the Monte-Carlo simulations we find that the levels of the errors in the HMI data lead to uncertainties in the horizontal electric field of 13% to 18%, that result in errors in the vertical Poynting flux of around 14%. If we add those uncertainties to the errors that we found when testing the PDFI method ( $< 25\%$  in  $S_z$ , Kazachenko et al. (2014)), then we end up with 14% to 29% error in the vertical Poynting flux depending on the LOS angle. Also, since some free energy might have been lost by flares prior to the X2.2 flare, we view the PDFI estimates of the free energy injected through the photosphere to be upper limits on the total free energy available before the flare.

This study is the first application of the PDFI electric field inversion technique to photospheric vector magnetic field and Doppler measurements. We find that the total amount of energy and helicity injected through the photosphere before the flare estimated from the PDFI method is consistent with estimates from other approaches, in spite of differing techniques. This agreement is very promising, implying that the PDFI technique is not only capable of describing the coronal energy and helicity budget, but can also provide instantaneous estimates of energy and helicity transferred through the photosphere.

We believe that both the derived dataset of PDFI electric fields and the PDFI method itself will be useful to the science community for analysis of the evolution and



spatial distribution of the photospheric electric fields, fluxes of energy and helicity, and their relationships with flare activity. In addition, PDFI electric fields can be used as time-dependent boundary conditions for data-driven models of coronal magnetic field evolution. The dataset for AR 11158 is available for downloading on our website<sup>2</sup>.

---

<sup>2</sup><http://cgem.stanford.edu>

## A. SCALING B AND E TO CARTESIAN MERCATOR MESH

The data we analyze have been reprojected, via Mercator reprojection, into a local, Cartesian coordinate system centered on AR 11158. The distortion of pixel scales from this reprojection has implications for inferring electric fields from magnetic evolution that we describe in detail here.

When observed magnetic fields are reprojected from the Sun’s spherical surface onto a plane using a conformal (shape-preserving) mapping, pixel areas in different regions of the reprojected coordinate system generally do not correspond to the same physical areas on the Sun. Denoting the area of pixel  $ij$  on the Sun as  $A_{ij}^S$ , and in the mapped coordinates as  $A_{ij}^M$ ,  $A_{ij}^M \approx A_{ij}^S$  near the center of the reprojection, but  $A_{ij}^M \neq A_{ij}^S$  far from center. In contrast, the reprojection does not directly alter the magnetic field values themselves: the fields are interpolated onto the reprojected grid point, but the interpolation attempts to faithfully represent measured field values at each interpolated point. While observed magnetic field vector data have units of field strength, i.e. gauss, they are more accurately described as measurements of pixel-averaged flux densities,  $\text{Mx}/\text{cm}^2$ . This is because the flux in pixel  $ij$  could be confined within a subregion of the pixel with fraction area  $f_{ij}A_{ij}^S$ , where the fill fraction  $f_{ij}$  obeys  $0 < f_{ij} < 1$ , implying a true field strength  $B^{\text{true}} = B^{\text{app}}/f$  larger than the apparent field strength (“pixel-averaged flux density”)  $B^{\text{app}}$  measured by the instrument.

The question, however, arises: Do we need to modify the field strengths in the reprojected system – call the original field strengths  $\mathbf{B}^S$ , and the reprojected field strengths  $\mathbf{B}^M$  – to account for the distorted areas? If so, how? Do  $B_n$  and the horizontal magnetic field components,  $\mathbf{B}_h$  need to be compensated in the same way? How should velocities and electric fields be modified to compensate for this distortion?

For concreteness, we can consider these questions in the context of the reprojection that we use for solar observations, the Mercator projection (Welsch et al. 2009). Briefly, the

distortion of scale in Mercator projections is a function of latitude alone. The horizontal Mercator coordinate,  $x$ , is mapped one-to-one with the heliocentric longitude,  $\phi$ , and is independent of latitude. Because the distance between lines of constant longitude decreases with increasing latitude, the projection’s scale (the physical distance corresponding to a fixed distance in the projected image) must decrease (fewer solar Mm per Mercator pixel) with increasing latitude. As lines of constant longitude converge toward the poles on a spherical surface, the physical distance between such lines tends to zero. In Mercator coordinates, however, the distance between two lines of constant longitude  $\Delta x$ , is fixed, independent of latitude  $\theta$ . Effectively, this means the projection magnifies distances toward the poles. (This effect is easily seen on Mercator projections of the Earth’s surface, on which Antarctica and Greenland, for example, appear too large relative to landmasses at lower latitudes.) Consequently, to preserve conformality, displacements in the vertical Mercator coordinate,  $dy$ , corresponding to a fixed latitudinal displacement  $d\theta$ , increase toward the poles. Because the physical length corresponding to a fixed  $d\theta$  shrinks toward the poles as  $1/\cos(\theta)$ , and  $dx$  scales in the same way (via conformality), pixel areas in the reprojected system are scaled by  $\cos^2(\theta)$  compared to areas on the Sun.

Consider two reprojected pixels with the same normal magnetic field, one at high latitude and one at low latitude, denoting these  $B_n^H = B_n^L$  respectively. These have the same fluxes in the projection,  $\Phi^{M,H} \approx \Phi^{M,L}$ . The flux in each reprojected pixel, however, corresponds to differing fluxes on the Sun:  $\Phi^{M,L} \approx \Phi^{S,L}$ , but  $\Phi^{S,H} < \Phi^{M,H}$  since the actual solar area corresponding to high-latitude pixels is smaller. We choose to handle this by multiplying  $B_n$  in each reprojected pixel by  $\cos^2(\theta)$ , to compensate for distortion of its area as a function of latitude; at the same time, we do not rescale pixel legths.

When flux emerges into a pixel,  $v_n$  transports horizontal field  $B_h$  along a pixel edge of length  $L$  over a time interval  $\Delta t$ , meaning  $\Phi_{em} = v_n L B_h \Delta t$  has emerged. This means

the normal flux in the pixels who share this edge must change by  $\Phi_{em}$ , to account for the emerged flux; we have assumed that flux in each pixel straddling  $L$  has been compensated by a factor of  $\cos^2(\theta)$ . For the emerged horizontal flux to match the changes in vertical flux, two factors of  $\cos(\theta)$  must be present in the product  $v_n B_h$ , since we are not rescaling  $L$ . We can scale  $v_n$  by  $\cos^\alpha(\theta)$  and  $B_h$  by  $\cos^\beta(\theta)$ , which yields

$$\alpha + \beta = 2. \tag{A1}$$

When flux is horizontally transported from one pixel to another,  $v_h$  transports vertical field  $B_n$  across a pixel edge of length  $L$  over a time interval  $\Delta t$ , meaning a flux  $\Phi_{xport} = v_h L B_n \Delta t$  has been moved. This means the normal fluxes in the pixels who share this edge must each change by  $\Phi_{xport}$ , to account for the transported flux. Because  $B_n$  has already been rescaled by  $\cos^2\theta$ ,  $v_h$  in the product  $v_h L B_n$  does not need any scaling.

The scaling of the vertical Poynting flux  $S_z = (E_h \times B_h)$  with latitude can provide additional constraints. Given estimates of  $cE_h$  and  $B_h$  with the same values in high- and low- latitude Mercator pixels, the pixel-integrated Poynting flux at high latitude must be scaled by  $\cos^2(\theta)$ , to account for the area distortion. Recall that  $cE_h$  is proportional to the sum of  $v_n B_h$ , scaled by  $\cos^{\alpha+\beta}(\theta)$ , and  $v_h B_n$ , already scaled by  $\cos^2(\theta)$ . Because  $S_z$  must scale as  $\cos^2(\theta)$  for any  $v$ , we can consider the special case  $v_h = 0$ , implying  $S_z = v_n B_h^2$ , so

$$\alpha + 2\beta = 2. \tag{A2}$$

Comparing equations A1 and A2 implies  $\beta = 0$ , so  $B_h$  is unscaled, but  $\alpha = 2$ , so  $v_n$  is scaled by  $\cos^2(\theta)$ . Physically, this implies that the vertical transport of emerging flux at high latitudes is scaled to make sure a “scaled amount” of flux emerges. This scaling implies that  $E_h$  is automatically and implicitly scaled (via scaling applied to  $B_n$  and  $v_n$ ) by  $\cos^2(\theta)$ , and that  $E_z = v_h \times B_h$  is unscaled.

Summarizing the above, we scale  $B_n, v_n, E_h$  by  $\cos^2(\theta)$  and do not scale  $B_h, v_h, E_n$ .

## REFERENCES

- Abbett, W. P., Z. Mikić, J. A. Linker, J. M. McTiernan, T. Magara, and G. H. Fisher: 2004. *JASTP* **66**, 15.
- Alissandrakis, C. E.: 1981. *A&A* **100**, 197.
- Alvarado-Gómez, J. D., J. C. Buitrago-Casas, J. C. Martínez-Oliveros, C. Lindsey, H. Hudson, and B. Calvo-Mozo: 2012. *Sol. Phys.* **280**, 335.
- Aschwanden, M. J. and A. W. Sandman: 2010. *AJ* **140**, 723.
- Aschwanden, M. J., X. Sun, and Y. Liu: 2014. *ApJ* **785**, 34.
- Berger, M. A.: 1984. *Geophysical and Astrophysical Fluid Dynamics* **30**, 79.
- Berger, M. A. and G. B. Field: 1984. *Journal of Fluid Mechanics* **147**, 133.
- Borrero, J. M., S. Tomczyk, M. Kubo, H. Socas-Navarro, J. Schou, S. Couvidat, and R. Bogart: 2011. *Sol. Phys.* **273**, 267.
- Cheung, M. C. M. and M. L. DeRosa: 2012. *ApJ* **757**, 147.
- Chintzoglou, G. and J. Zhang: 2013. *ApJ* **764**, L3.
- Dalmasse, K., E. Pariat, G. Valori, P. Démoulin, and L. M. Green: 2013. *A&A* **555**, L6.
- Deng, N., Y. Xu, G. Yang, W. Cao, C. Liu, T. R. Rimmele, H. Wang, and C. Denker: 2006. *ApJ* **644**, 1278.
- Fisher, G. H. and B. T. Welsch: 2008. In: R. Howe, R. W. Komm, K. S. Balasubramaniam, and G. J. D. Petrie (eds.): *Subsurface and Atmospheric Influences on Solar Activity*, Vol. 383 of *Astronomical Society of the Pacific Conference Series*. p. 373.
- Fisher, G. H., B. T. Welsch, and W. P. Abbett: 2012. *Sol. Phys.* **277**, 153.

- Fisher, G. H., B. T. Welsch, W. P. Abbett, and D. J. Bercik: 2010. *ApJ* **715**, 242.
- Fu, Y. and B. T. Welsch: 2015. *ArXiv e-prints*.
- Georgoulis, M. K., K. Tziotziou, and N.-E. Raouafi: 2012. *ApJ* **759**, 1.
- Gosain, S.: 2012. *ApJ* **749**, 85.
- Hoeksema, J. T., Y. Liu, K. Hayashi, X. Sun, J. Schou, S. Couvidat, A. Norton, M. Bobra, R. Centeno, K. D. Leka, G. Barnes, and M. Turmon: 2014. *Sol. Phys.* **289**, 3483.
- Hudson, H. S., G. H. Fisher, and B. T. Welsch: 2008. In: R. Howe, R. W. Komm, K. S. Balasubramaniam, and G. J. D. Petrie (eds.): *Subsurface and Atmospheric Influences on Solar Activity*, Vol. 383 of *Astronomical Society of the Pacific Conference Series*. p. 221.
- Janvier, M., G. Aulanier, V. Bommier, B. Schmieder, P. Démoulin, and E. Pariat: 2014. *ApJ* **788**, 60.
- Jiang, Y., R. Zheng, J. Yang, J. Hong, B. Yi, and D. Yang: 2012. *ApJ* **744**, 50.
- Jing, J., S.-H. Park, C. Liu, J. Lee, T. Wiegmann, Y. Xu, N. Deng, and H. Wang: 2012. *ApJ* **752**, L9.
- Jing, J., J. Qiu, J. Lin, M. Qu, Y. Xu, and H. Wang: 2005. *ApJ* **620**, 1085.
- Kazachenko, M. D., G. H. Fisher, and B. T. Welsch: 2014. *ApJ* **795**, 17.
- Keller, C. U., J. W. Harvey, and M. S. Giampapa: 2003. In: S. L. Keil and S. V. Avakyan (eds.): *Innovative Telescopes and Instrumentation for Solar Astrophysics*, Vol. 4853 of *Society of Photo-Optical Instrumentation Engineers (SPIE) Conference Series*. pp. 194–204.

- Kosugi, T., K. Matsuzaki, T. Sakao, T. Shimizu, Y. Sone, S. Tachikawa, T. Hashimoto, K. Minesugi, A. Ohnishi, T. Yamada, S. Tsuneta, H. Hara, K. Ichimoto, Y. Suematsu, M. Shimojo, T. Watanabe, S. Shimada, J. M. Davis, L. D. Hill, J. K. Owens, A. M. Title, J. L. Culhane, L. K. Harra, G. A. Doschek, and L. Golub: 2007. *Sol. Phys.* **243**, 3.
- Leka, K. D., G. Barnes, A. D. Crouch, T. R. Metcalf, G. A. Gary, J. Jing, and Y. Liu: 2009. *Sol. Phys.* **260**, 83.
- Lites, B. W., D. L. Akin, G. Card, T. Cruz, D. W. Duncan, C. G. Edwards, D. F. Elmore, C. Hoffmann, Y. Katsukawa, N. Katz, M. Kubo, K. Ichimoto, T. Shimizu, R. A. Shine, K. V. Streander, A. Suematsu, T. D. Tarbell, A. M. Title, and S. Tsuneta: 2013. *Sol. Phys.* **283**, 579.
- Liu, C., N. Deng, R. Liu, J. Lee, T. Wiegmann, J. Jing, Y. Xu, S. Wang, and H. Wang: 2012a. *ApJ* **745**, L4.
- Liu, J. and H. Zhang: 2006. *Sol. Phys.* **234**, 21.
- Liu, Y., J. T. Hoeksema, P. H. Scherrer, J. Schou, S. Couvidat, R. I. Bush, T. L. Duvall, K. Hayashi, X. Sun, and X. Zhao: 2012b. *Sol. Phys.* **279**, 295.
- Liu, Y. and P. W. Schuck: 2012. *ApJ* **761**, 105.
- Longcope, D. W. and B. T. Welsch: 2000. *ApJ* **545**, 1089.
- Malanushenko, A., C. J. Schrijver, M. L. DeRosa, and M. S. Wheatland: 2014. *ApJ* **783**, 102.
- Maurya, R. A., P. Vemareddy, and A. Ambastha: 2012. *ApJ* **747**, 134.
- Melrose, D. B.: 1995. *ApJ* **451**, 391.



- Metcalf, T. R., R. C. Canfield, H. S. Hudson, D. L. Mickey, J.-P. Wulser, P. C. H. Martens, and S. Tsuneta: 1994. *ApJ* **428**, 860.
- Pesnell, W. D., B. J. Thompson, and P. C. Chamberlin: 2012. *Sol. Phys.* **275**, 3.
- Petrie, G. J. D.: 2012. *Sol. Phys.* p. 183.
- Petrie, G. J. D.: 2013. *Sol. Phys.* **287**, 415.
- Poletto, G. and R. A. Kopp: 1986. In: D. F. Neidig (ed.): *The Lower Atmospheres of Solar Flares*. pp. 453–465, National Solar Observatory.
- Priest, E. R. and T. G. Forbes: 2000, *Magnetic Reconnection. MHD theory and applications*. Cambridge University Press.
- Qiu, J., J. Lee, D. E. Gary, and H. Wang: 2002. *ApJ* **565**, 1335.
- Qiu, J., H. Wang, C. Z. Cheng, and D. E. Gary: 2004. *ApJ* **604**, 900.
- Sakurai, T.: 1989. *Space Sci. Rev.* **51**, 11.
- Schou, J., P. H. Scherrer, R. I. Bush, R. Wachter, S. Couvidat, M. C. Rabello-Soares, R. S. Bogart, J. T. Hoeksema, Y. Liu, T. L. Duvall, D. J. Akin, B. A. Allard, J. W. Miles, R. Rairden, R. A. Shine, T. D. Tarbell, A. M. Title, C. J. Wolfson, D. F. Elmore, A. A. Norton, and S. Tomczyk: 2012. *Sol. Phys.* **275**, 229.
- Schrijver, C. J., G. Aulanier, A. M. Title, E. Pariat, and C. Delannée: 2011. *ApJ* **738**, 167.
- Schuck, P. W.: 2006. *ApJ* **646**, 1358.
- Schuck, P. W.: 2008. *ApJ* **683**, 1134.
- Sun, X., J. T. Hoeksema, Y. Liu, T. Wiegelmann, K. Hayashi, Q. Chen, and J. Thalmann: 2012. *ApJ* **748**, 77.

- Tarr, L., D. Longcope, and M. Millhouse: 2013. *ApJ* **770**, 4.
- Tsuneta, S., K. Ichimoto, Y. Katsukawa, S. Nagata, M. Otsubo, T. Shimizu, Y. Suematsu, M. Nakagiri, M. Noguchi, T. Tarbell, A. Title, R. Shine, W. Rosenberg, C. Hoffmann, B. Jurcevich, G. Kushner, M. Levay, B. Lites, D. Elmore, T. Matsushita, N. Kawaguchi, H. Saito, I. Mikami, L. D. Hill, and J. K. Owens: 2008. *Sol. Phys.* **249**, 167.
- Tziotziou, K., M. K. Georgoulis, and Y. Liu: 2013. *ApJ* **772**, 115.
- Vemareddy, P., A. Ambastha, and R. A. Maurya: 2012a. *ApJ* **761**, 60.
- Vemareddy, P., A. Ambastha, R. A. Maurya, and J. Chae: 2012b. *ArXiv e-prints*.
- Wang, H., J. Qiu, J. Jing, T. J. Spirock, V. Yurchyshyn, V. Abramenko, H. Ji, and P. R. Goode: 2004. *ApJ* **605**, 931.
- Wang, H., J. Qiu, J. Jing, and H. Zhang: 2003. *ApJ* **593**, 564.
- Wang, S., C. Liu, N. Deng, and H. Wang: 2014. *ApJ* **782**, L31.
- Wang, S., C. Liu, R. Liu, N. Deng, Y. Liu, and H. Wang: 2012. *ApJ* **745**, L17.
- Welsch, B. T.: 2006. *ApJ* **638**, 1101.
- Welsch, B. T. and G. H. Fisher: 2015. *ArXiv e-prints*.
- Welsch, B. T., G. H. Fisher, and X. Sun: 2013. *ApJ* **765**, 98.
- Welsch, B. T., Y. Li, P. W. Schuck, and G. H. Fisher: 2009. *ApJ* **705**, 821.
- Wiegelmann, T.: 2004. *Sol. Phys.* **219**, 87.